



FEDERAL UNIVERSITY OF SANTA CATARINA
MECHANICAL ENGINEERING DEPARTMENT
MATERIALS ENGINEERING

Bachelor Thesis from
BRUNO TOSELLI

Direct-ink writing of PDC-based SiOC anodes for microbial fuel cells

Developed at University of Bremen,
Advanced Ceramics Institute

Bremen - Germany
2022

FEDERAL UNIVERSITY OF SANTA CATARINA
MECHANICAL ENGINEERING DEPARTMENT
MATERIALS ENGINEERING

Diploma thesis from
BRUNO TOSELLI

Direct-ink writing of PDC-based SiOC anodes for microbial fuel cells

Thesis presented to the Bachelor Course
Materials Engineering from the Federal
University of Santa Catarina as a requisite to
obtain the title "Materials Engineer".

Supervisors:
Pedro Henrique da Rosa Braun
Dr. rer. nat. Michaela Wilhelm

Bremen - Germany
2022

FEDERAL UNIVERSITY OF SANTA CATARINA
MECHANICAL ENGINEERING DEPARTMENT
MATERIALS ENGINEERING

BRUNO TOSELLI

Direct-ink writing of PDC-based SiOC anodes for microbial fuel cells

This work was assessed adequate to the attainment of the title – “Materials Engineer” and approved by the Graduation Course of Materials Engineering from Federal University of Santa Catarina.

Prof. Dylton do Vale Pereira Filho,
TCC Coordinator

Assessment Committee:

Dr.rer.nat. Michaela Wilhelm

Pedro Henrique da Rosa Braun

Toselli, Bruno, 1996.

Direct-ink writing of PDC-based SiOC anodes for microbial fuel cells
/ Bruno Toselli. - 2022.

61 f.: il color. ; 30 cm

Supervisor: Pedro Henrique da Rosa Braun

Co-supervisor: Dr. rer. nat. Michaela Wilhelm

Trabalho de Conclusão de Curso – Universidade Federal de Santa Catarina,
Curso de Graduação em Engenharia de Materiais, 2022.

1. Polymer Derived Ceramics (PDC). 2. Microbial Fuel Cells (MFC). 3. Direct Ink Writing (DIW). I. Toselli, Bruno. II. Federal University of Santa Catarina. Materials Engineering bachelor. III. Direct-ink writing of PDC-based SiOC anodes for microbial fuel cells.

Acknowledgment

I dedicate this moment to briefly express my gratitude for the international experience of this bachelor thesis.

Therefore, I must first highlight the Advanced Ceramics Institute, for granting me such an opportunity and allowing me the freedom to enjoy all its infrastructure, its team and, above all, its knowledge and technologies, which make it an excellent environment for development. Factors that reinforce the magnitude of the positive impact on the professional career.

During the entire period, I received assistance and was able to learn from the various collaborators, not only from my research, but from the entire institute, from its various lines of research, with national and international impact. Without it, my development, execution of the various activities and results would not be possible.

Since the beginning of the internship, the head of the institute, Kuroschi Rezwan, the intermediary, Renato de Almeida and my research supervisors, Michaela Wilhelm and Pedro Henrique da Rosa Braun, insisted on offering a healthy and friendly environment, in order to promote the proliferation, not only from the findings of ideas, suggestions and improvements, but also from their application. In addition to monitoring and availability when necessary and great support in various issues.

I could not fail to mention the infrastructure of UFSC (Federal University of Santa Catarina), reflected mainly through the internship coordinator, Marcus Barnette and Bruno Alexandre de Castro Henrique. Both were readily available to assist in the various topics involved, from the prospect of internship vacancies, through monitoring during the execution and extending to the end of the experience. Without this, the existence and maintenance of these great opportunities for internships and researches that we have as students of materials engineering would be unfeasible.

As my mother likes to do, likes to save the best for last, I wait for the end to thank my family, the most important safe haven and base that could maintain all the achievements I had throughout my all journey so far during, not only the studies and university, but mostly as a human being. Adriana Fiorelli, Milena Toselli, Fabio Toselli and in memoriam of the matriarch of our family, Maria Amélia, I love you with all my heart.

Dedication

I
dedicate
this bachelor's thesis
to my maternal and paternal
grandmothers, Maria Amélia and
Mirair Aparecida, respectively. Especially
my maternal grandma, who raised and took care
of me, so that I can be here today, moving up to the next
level of my journey. During the development and writing of this work,
both passed away towards to **the other plane** and I know that from there they
are going through eternity in a lighter, happier and painless way, looking
out for us, ensuring that the family created with so much love and
affection continues to prosper. I will continue to make you
proud, living an abundant life, taking your lessons,
to be able to raise my own family with the
love, care and protection that I
received. Love you
forever



ABSTRACT

Among many applications of porous polymer-derived ceramics (PDCs), when used in microbial fuel cells (MFCs) they can lead to appropriate performance due to the possibility of tailoring the surface properties of the material used as electrode. One of the limitations is the pore clogging during biofilm formation which can be solved by using direct-ink writing (DIW) processing instead of tape-casting. In this work a PDC-based SiOC ink composition used in previous work for tape-casting was adapted to DIW method. These 3D structures will be used later as MFCs anodes to avoid pore clogging and enhance current density. Additionally, the influence of azodicarbonamide on the formation of surface pores was studied. The inks were produced via DIW using 580 μm nozzle diameter or tape-casting, followed by drying at room temperature and pyrolysis at 1000°C for the ceramic conversion of the green bodies. To obtain the ideal viscosity to DIW and print structures that did not collapsed even after layer-by-layer addition, the solid loading of the ink was increased from 70 to 85 wt.% increasing the yield point from 25.87 ± 2.24 to 1141.33 ± 32.33 Pa. Results from scanning electron microscope, mercury intrusion porosimetry and nitrogen adsorption indicate a pore structure of the produced samples with an average pore window size ranging from 0.21 to 105 μm , being higher the lower the solid loading is, and a specific surface area from 21.95 to 82.51 m^2g^{-1} , being higher the lower the azodicarbonamide is and when using DIW method processing. These finding are a good indicative to the adequate biofilm formation during further MFC applications. The functional properties were assessed by vapor adsorption, electrochemical spectroscopy and chemical stability analysis. All samples showed a hydrophilic behavior and chemical stability independent of the method, solid loading or amount of azodicarbonamide used. The electrical conductivity ranged from 0.57 ± 0.01 to 1.89 ± 0.32 Sm^{-1} , being higher the lower the azodicarbonamide amount is. Lastly, even after increasing the azodicarbonamide from 17 to 29 wt.% in solid phase, the open porosity on the surface still remained mostly the same. Overall, the obtained PDC-based SiOC ink could be adapted to the DIW and proved to be promising to be applied as anodes for MFC in the future.

Keywords: Polymer-derived ceramics (PDC), microbial fuel cells (MFC), direct ink writing (DIW)

RESUMO

Dentre as diversas aplicações das cerâmicas derivadas de polímeros (PDCs) porosas, quando utilizadas em células a combustível microbianas (MFCs) podem levar a um desempenho adequado devido à possibilidade de ajustar as propriedades superficiais do material utilizado como eletrodo. Uma das limitações é o entupimento dos poros durante a formação do biofilme, que pode ser resolvido usando o processamento de escrita direta a tinta (DIW) em vez de tape-casting. Neste trabalho, uma composição de tinta SiOC baseada em PDC usada em trabalhos anteriores para tape-casting foi adaptada ao método DIW. Essas estruturas 3D serão usadas como anodo de MFC para evitar o entupimento dos poros e aumentar a densidade de corrente. Além disso, foi estudada a influência do azodicarbonamida (AZO) na formação de poros superficiais. As tintas foram produzidas via DIW utilizando bico de 580 μm de diâmetro ou tape-casting, seguido de secagem em temperatura ambiente e pirólise a 1000°C para conversão cerâmica dos corpos verdes. A viscosidade ideal para DIW ao imprimir estruturas que não colapsam mesmo após a adição de camadas, a carga sólida da tinta foi aumentada de 70 para 85% em peso, aumentando o yield point de $25,87 \pm 2,24$ para $1141,33 \pm 32,33$ Pa. Resultados de microscopia eletrônica de varredura, porosimetria de intrusão de mercúrio e adsorção de nitrogênio indicam uma estrutura porosa com tamanho médio de poros variando de 0,21 a 105 μm , sendo maior quanto menor a carga sólida, além de uma área superficial específica de 21,95 a 82,51 m^2g^{-1} , sendo maior quanto menor a quantidade de AZO e quando se utiliza o método de processamento DIW. Tais análises representam bom indicativo da formação adequada de biofilme. As propriedades funcionais foram avaliadas por adsorção de vapor, espectroscopia eletroquímica e estabilidade química. Todas as amostras foram hidrofílicas e quimicamente estáveis, independente do método, carga sólida ou quantidade de AZO utilizada. A condutividade elétrica variou de $0,57 \pm 0,01$ a $1,89 \pm 0,32$ Sm^{-1} , sendo maior quanto menor a quantidade de AZO. Por fim, mesmo após aumentar o AZO de 17 para 29% em peso na fase sólida, a porosidade permaneceu com poucas alterações. No geral, a tinta SiOC baseada em PDC obtida pode ser adaptada ao DIW e provou-se promissora para ser aplicada como anodo em MFC.

Palavras-chave: Cerâmicas derivadas de polímeros, células combustíveis microbianas, escrita de tinta direta.

LIST OF FIGURES

Figure 1 - Main classes of Si-polymer as precursors for ceramics. Source: [21].	4
Figure 2 - Polymer to ceramic transformation according to the temperature. Source: Adapted from [21].	5
Figure 3 - Schematic diagram of a typical two-chamber microbial fuel cell. Source: [28].	7
Figure 4 - (a-c) Optical and SEM images of SiC 3D scaffolds (16 layers) printed with 400 μm nozzles, (d-g) 3D models and optical images of various 3D struts (32 layers) prepared through a 200 μm nozzle with polycarbosilane/n-hexane filament [61].	12
Figure 5 - Diagram of the sample's preparation step by step. Source: Author.	15
Figure 6 - Labeling system of the samples analyzed in this work, presenting the three terms that define them and their modifications studied respectively. Source: Author.	16
Figure 7 - Scheme of the rotational rheometer technique used with plate-plate geometries. Source: [64].	17
Figure 8 - Graph representation of the yield point. Source: Author.	17
Figure 9 - Isotherms classification by IUPAC. Source: [67].	19
Figure 10 - The sample shape on right side and the contacted configuration during EIS measurement. Source: Author.	22
Figure 11 - Left) Three 3D samples using solid loading of 70 wt.% and lattice cuboid geometry. Right) 3D printing samples using solid loading of 75 wt.% and lattice cylindroid geometry. Source: Author.	24
Figure 12 – Left) Rheological behavior curve using solid loading of 70 wt.% and shear rate ramp test. Right) Rheological behavior curve using solid loading of 75 wt.% and shear rate ramp test. Source: Author.	25
Figure 13 – Rheological behavior curve using solid loading of 80 wt.% and shear rate ramp test. Source: Author.	26
Figure 14 – Left) Syringe test using solid loading of 80 wt.%. Right) 3D printed samples with the same loading. Source: Author.	26
Figure 15 – Left) 3D printing using solid loading of 85 wt.% showing the layer-by-layer of a lattice cylindroid geometry. Right) 3D printing using solid loading of 85 wt.% of the same sample, but showing the top view and its infill. Source: Author.	27

Figure 16 - Rheological behavior curve using solid loading of 85 wt.% and shear rate ramp test. Source: Author.....	27
Figure 17 - Different views of 3D structure using AZO at 17, 23 and 29 wt.%. a) surface view in 500x magnification of AZO at 17%; b) cross-section view in 500x magnification of AZO at 17%; c) surface view in 500x magnification of AZO at 23%; d) cross-section view in 500x magnification of AZO at 23%; e) surface view in 500x magnification of AZO at 29%; f) cross-section view in 500x magnification of AZO at 29%. Source: Author.....	28
Figure 18 - Different views of tape-casting structure using 70.8 and 85 wt.%. a) surface view in 500x magnification of 70.8%; b) cross-section view in 500x magnification of 70.8%; c) surface view in 500x magnification of 85%; and d) cross-section view in 500x magnification of 85%. Source: Author.	29
Figure 19 - Layer-by-layer view of the 3D structure with 85 wt.%. Source: Author....	30
Figure 20 - Pore window size distribution and open porosity from Hg intrusion porosimetry. Source: Author.....	31
Figure 21 - Specific surface area of the samples from BET method. Source: Author.	32
Figure 22 - Nitrogen adsorption/desorption isotherms of the samples. Source: Author.	33
Figure 23 - Vapor adsorption by water and n-heptane solvents and its ratio. Source: Author.....	34
Figure 24 - Electrical conductivity and its standard deviation from EIS. Source: Author.	35
Figure 25 - Chemical stability under PBS solution with pH 7 over 4 weeks. Source: Author.....	36

LIST OF TABLES

Table 1 - Comparison of traditional and advanced ceramics. Source: Adapted from [18].	3
Table 2 - Weight fraction of each component in solid loading. Source: Adapted from [16].	14
Table 3 – Analysis and measurements to evaluate the samples and its purpose. Source: Author.	16
Table 4 - Yield points of different solids loading from shear stress ramp rheological test. Source: Author.	25
Table 5 - Average pore window size and open porosity from Hg intrusion porosimetry. Source: Author.	31
Table 6 - Electrical conductivity and its standard deviation from EIS. Source: Author.	36

TABLE OF CONTENTS

1. INTRODUCTION	1
2. BACKGROUND LITERATURE	3
2.1 Polymer-derived ceramics (PDC)	3
2.2 Microbial Fuel Cells (MFCs)	6
2.2.1 Anode	8
2.3 Additive Manufacturing	8
2.3.1 Direct Ink Writing	10
2.3.2 PDC manufacturing by DIW	11
3. AIM AND APPROACH	13
4. MATERIALS AND METHODS	14
4.1 Sample Preparation	14
4.1.1 Samples Labeling	15
4.2 Analysis and measurements	14
4.2.1 Rheology behavior	16
4.2.2 Scanning Electron Microscopy	18
4.2.3 Mercury Intrusion Porosimetry	18
4.2.4 Nitrogen Adsorption	19
4.2.5 Vapor Adsorption	20
4.2.6 Electrochemical Impedance Spectroscopy	21
4.2.7 Chemical Stability	22
5. RESULTS AND DISCUSSION	24
5.1 3D Printing Optimization	24
5.2 Surface Structure	24
5.3 Pore Structure	30
5.4 Functional Properties	33

6. CONCLUSION.....	37
7. OUTLOOK.....	39
REFERENCES.....	40
APENNDIX A – History Of The Institute.....	47
APENNDIX B – Timetable Schedule.....	48

1. INTRODUCTION

Over the last 50 years, when oil was discovered to be an exhaustible energy source, a race began for new sources of renewable energy to replace it and minimize its damage to the environment. In order to face these problems and deal with the new demands that have arisen [1], technologies and devices such as microbial fuel cells (MFCs) were developed [2].

A simple system that uses biomass energy from wastewater and, through the interaction of an electrode with the electroactive microorganism, mainly represented by bacteria, is able to convert this chemical energy into electrical energy while treating this water [3, 4]. To the efficiency of an MFC, the anode-bacteria interface must show good interaction, through the surface roughness, biocompatibility of the anode. For a higher MFC performance, the anode should also possess good electrical conductivity and chemical stability [5, 6].

Carbon-based electrodes are commonly used due to their high conductivity, however, they have low thermal and chemical stability, compromising the lifespan of cells under operating conditions [7]. Thus, ceramic materials are a great alternative to replace carbon-based anodes, according to their thermal and chemical stability [8, 9], especially polymer-derived ceramics (PDCs) due to the possibility of adding conductive fillers during their synthesis to supply the low electrical conductivity [10], and the use of pre-ceramic precursors that guarantee the necessary surface properties to the final application [11, 12].

Therefore, the aim is to continue the researches [13, 14, 15] that use porous PDSs with electrical properties, synthesized from polysiloxanes as precursor to create an anode with the desired chemical and physical properties for microbial fuel cells (MFCs).

Based on the parameters such as pyrolysis temperature and composition of solid phase conditions, from the research by da Rosa Braun et al, 2021 [16], optimizations will be made by means of solid loading and amount of pore formation agent so the composition previously processed by tape-casting will be now processed using 3D printing, by the method of Direct-ink writing (DIW).

Then, it will be investigated the possibility of achieving, through the three-dimensional structures, a greater surface area of the sample that enables the adhesion

and homogeneous growth of bacterial colonization, preventing the pore clogging and promoting better values of electrical properties to enhance the MFC performance.

2. BACKGROUND LITERATURE

2.1 Polymer-derived ceramics (PDC)

Ceramics are the oldest materials processed by humans, so over the millenniums many changes occurred, opening space for the advanced ceramics development. They differ from the traditional ceramics in distinctive aspects, such as raw materials, processing, properties, application and others as Table 1 shown [17, 18].

Table 1: Comparison of traditional and advanced ceramics. Source: Adapted from [18].

Characteristics	Traditional	Advanced
Raw material	Naturally occurring ores, minerals with no or little processing (sand, clay, feldspar, quartz)	Extensively processed materials (alumina, zirconia, titania, silicon nitride, sialon)
Processing	Dry pressing, extrusion, slip casting, drying, firing (often more than once), finishing	Doctor blade, pressing (hot, isostatic and hot isostatic), injection molding, controlled in situ oxidation, sintering (low temperature, fast cycle), automation
Properties	Thermal expansion, conductivity, mechanical strength	Mechanical strength, fracture toughness, electrical conductivity, optical, dielectric and magnetic properties
Application	Refractories, crockery, sanitaryware, sheet glass	Ceramic engineers, dielectrics and piezoelectric, magnetics, electrooptic, opto-electronics

Following the data of Table 1, advanced ceramics in general shows raw materials in higher purity, controlled size particles and distribution and use of dopants. Concerning about processing, the use of advanced ceramics allows go further than the basic route of grinding, mixing, fabrication, drying and firing, which is important since the basic route is limited by the green body properties, such as rheology and mechanic, in addition to requiring temperatures above than 1000°C during firing step [17, 18].

PDCs arise in order to overcome these by showing advantages in terms of processing temperature and methods, and the available resulting surface properties.

PDCs is a class of silicon-based ceramics originated from the controlled decomposition of silicon-based polymers. The main chain of the polymeric precursor is composed by silicon that can be bonded with hetero elements such as oxygen in polyorganosiloxanes, carbon in polycarbosilanes, nitrogen in -silazanes or boron in borosilanes [19].

The polymeric precursor is processed into a polymer-derived ceramic through cross-linking followed by pyrolysis. Thus, the properties of the final product are strongly dependent of the composition and structure of the preceramic polymer (PCP) and pyrolysis parameters. Therefore, it is possible to adjust the resulting pore structure and surface properties of the PDC by adjusting its molecular structure and the pyrolysis temperature and heating rate. Figure 1 depicts different molecular structures that PDC can show [19-21].

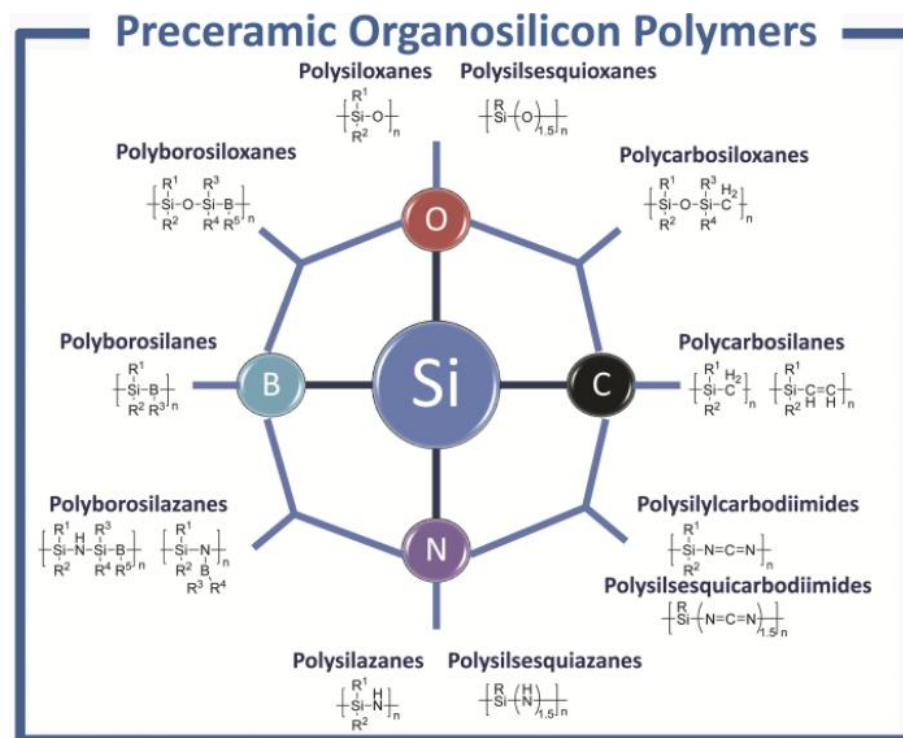


Figure 1: Main classes of Si-polymer as precursors for ceramics. Source: [21].

In order to achieve the desired final properties, it is important to comprehend each processing step, especially the reactions during pyrolysis [19].

At low temperatures up to 200 °C is possible to shape the low viscous preceramic polymer to afterwards being cured to maintain its structure, prevented to

be melted. To achieve a proper mechanical stability, the cross-linking step is necessary and can be made in by chemical and/or thermal crosslinking [19, 22].

In the next step chemical bonds are broken allowing rearrangement and releasing of organic functional groups, which is seen above 400 °C. Also, in the range of temperature 400 – 600 °C, and hybrid material is formed called “ceramer”, which shows the presence of both polymeric and ceramic phases. This process between the transition from organic to inorganic is marked by a weight loss of 10 to 30% and the creation of an amorphous PDC structure and is finished between 800 to 1000°C [22].

When increasing the temperature above 1000°C, an amorphous ceramic can start to. Figure 2 shows the microstructural evolution with pyrolysis temperature at each temperature highlighted [22].

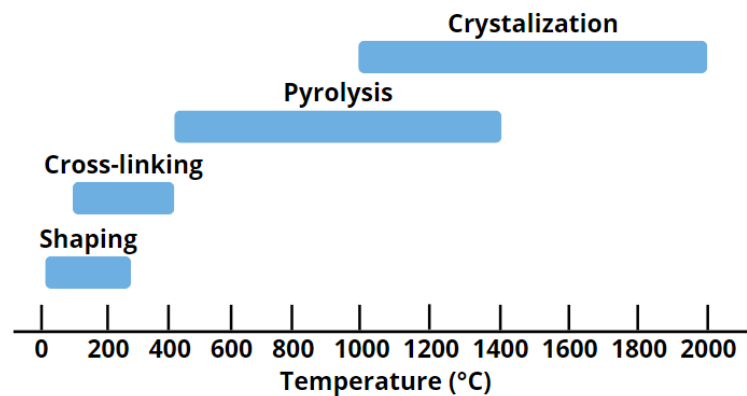


Figure 2: Polymer to ceramic transformation according to the temperature. Source: Adapted from [21].

Besides the pyrolysis parameters, it is also possible to add fillers in order to obtain certain properties to the resulting PDC. For example, Azodicarbonamide can be added as pore forming agent and graphite flakes or carbon black to improve the electrical conductivity. Therefore, by adjusting the pyrolysis parameters and chemical composition of the preceramic polymer, one can develop a PDC that can be useful in several in several fields, being find, among many areas, in energy and environmental systems [21].

Due to surface roughness, hydrophilicity, electrical conductivity and high specific surface area, PDCs are a promising class of material suited to the application in the field of Microbial fuel cells (MFC), once this technology requires the before-mentioned properties for bacterial attachment and electron transfer.

2.2 Microbial Fuel Cells (MFC)

Regarding the alternative sources of green energy, waste management and the climate changes happening around the globe, the continuously investigation for new technologies and developments keep growing towards new solutions finds, such as. Fuel cells. They have been studied for their implementation in many different environments to achieve presence in large-scale [23].

Its classification can be given mainly through three different groups, being catalytic, enzymatic and microbial. In which, the latter, know as microbial fuel cell (MFC), showed a strong increase in interest through research developed about it from the last two decades. MFCs are the only ones capable of generating electricity through chemical processes and reactions during interaction with microorganisms, thus converting this chemical energy into electrical energy [23].

Substrates used in MFC research vary from sugars and organic acids such as glucose or acetate to complex polymers such as starch and cellulose. Domestic, industrial, and animal waste streams have been used as feedstock for generating electricity in MFCs [23]. Basically, MFCs efficiently generate green energy from the treatment of different types of pollutants in wastewater [24].

The raw material used to generate electricity comes mainly from domestic, industrial and animal wastewater. In which, substrates such as sugars and organic acids are used, which can be glucose and organic acids, to complex polymers such as starch and cellulose [25].

Among many others, there are some groups of microorganisms in the contents of these wastewaters, which have characteristics of electricity production from respiration in the MFC chamber, such as *Firmicutes*, *Proteobacteria*, *Acidobacteria*, fungi and algae [24, 26, 27].

Known as a form of electrochemical fuel cell, MFCs consist of two main compartments: the anode and the cathode, which are commonly separated by a proton exchange membrane (PEM). On one hand, the anode chamber presents the microorganisms that oxidize the substrate, that is, the electron donor, while on the other hand, anaerobic oxidation is coupled with the release of electrons that are transported through the cellular respiratory chain to the anode [23]. Figure 3 shows a general scheme of a microbial fuel cell reactor.

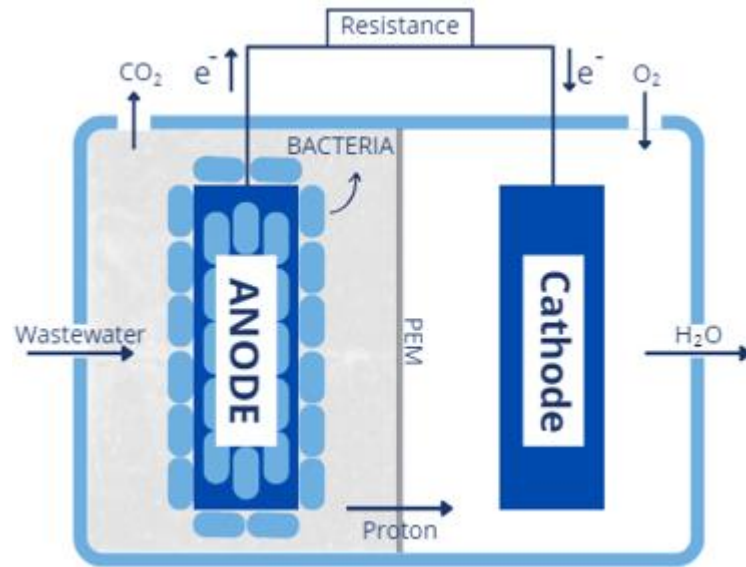
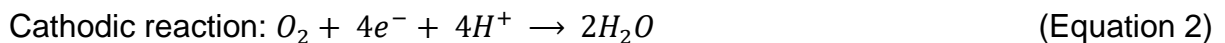
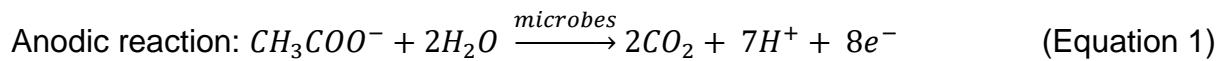


Figure 3: Schematic diagram of a typical two-chamber microbial fuel cell. Source: Adapted from [28].

Typically, the reactions that take place in the anode and cathode chamber when using acetate as a substrate can be described by equations 1 and 2 below [28].



From equations 1 and 2, it can be inferred that the general reaction occurs by breaking the substrate into carbon dioxide and water, thus generating the production of electricity as a by-product, which is used to feed an external circuit, promoting a flow of electricity. electrons from the anode to the cathode, turning the MFC into a bioreactor [28].

As mentioned earlier, some microorganisms have the ability to transfer electrons derived from the metabolism of organic matter to the anode. That is, in MFCs, bacterial species decompose different organic compounds and metallic complexes, in order to produce electrons and protons, which will strengthen the respiratory system itself and acquire the ability to produce a flow of electrons between the electrodes of the system [29]. Therefore, the key to understanding how to enhance the overall performance of an MFC is to understand the reactions that occurs at the anode, the requirements to promote better bacterial colonization and electrical conductivity [28].

2.2.1 Anode

To understand the theory of how MFCs work, it is of fundamental importance to understand the mechanism involved in the transfer of electrons from the anodic chamber. Microorganisms transfer electrons to the electrode through an electron transport system consisting of a series of components in the bacterial extracellular matrix or in conjunction with electron carriers dissolved in the bulk solution.

The performance of MFCs is strongly influenced by the selection of anodic and cathodic materials, in addition to the catalyst. Thus, an appropriate electrode is assigned: materials with high electrical conductivity, in order to boost electron transfer; high surface area, to increase sorption effects, as an example [30].

This shows that an ideal anode must have an optimized pore structure with high specific surface area and surface roughness for biofilm formation. The pore size on the surface must be large enough not only for the accommodation of bacteria, but also for the accessible transport of nutrients (from the substrate) to the biofilm. In addition, the electrical conductivity of the anode must be high to allow the transfer of electrons to the external circuit, connected to the cathode [31]. Therefore, the properties of the anode affect not only the rate of microbial adhesion activity, but also the rate of electron transfer in the cell [29].

From the moment that a given surface has narrow pore sizes, that is, below 500 μm , a scenario is established that increases the possibility of clogging of the pores, which leads to a limitation in mass transport. and consequent inefficiency in biofilm formation. It is known that larger pores are more favorable for proton transfer, as well as pH splitting. Despite being more prone to substrate loss and greater oxygen permeability [32]. In order to overcome these limitations, the possibility of using additive manufacturing processing, by selecting different 3D printing techniques, has been studied, thus being able to create anodes with pore sizes large enough to allow adequate mass transport at the anode [33].

2.3 Additive Manufacturing

Additive manufacturing (AM), also known as solid free form manufacturing (SFF), Rapid Prototyping (RP), or 3D printing, are a class of technologies in which a

piece is made directly from a three-dimensional virtual model, from the addition of material, contrary to subtractive manufacturing methodologies, such as traditional machining, characterized by extracting material from a block or billet [34]. According to ISO:ASTM 52900 (2015) [35], AM is defined as the set of technologies capable of aggregating materials in order to produce components from 3D models, conventionally manufactured by the deposition of layer-by-layer of material. Following this idea, AM differs from traditional processes and has the advantage of flexibility in the reproduction of different geometries [36].

To build a piece using the AM methodology, just a few steps and resources are necessary, being mainly, creating a 3D model, determining a 3D computational graphic, and selecting the materials that will be used in the processing. This greater simplicity provides the possibility of making pieces, without the need for adaptations due to the limitations of the processing method, thus being able to present geometries with greater complexity shapes [37]. Finished pieces can be manufactured, having the final physical properties required by the project requirements, but even those that require additional processing steps, that is, semi-finished ones, have also proved to be economically viable, promoting more application possibilities, even when they are more specialized [34].

AM is categorized into seven main techniques, as determined by the ISO:ASTM 52900 (2015) standard [35]: binder jetting (BJ), material jetting (MJ), material extrusion (ME), powder bed fusion (PBF), sheet lamination (SL), direct energy deposition (DEB) and vat photopolymerization (VP), within which each group has subcategories [38]. As an example, the material extrusion technique (ME) is given normally for the heating of input and selective release through a nozzle to form the 3D piece, where three processes can be mentioned within this category: Direct Ink Writing (DIW); Fused Deposition Modeling (FDM) and Fused Filament Fabrication (FFF) [39, 40].

A wide variety of metallic, polymeric and ceramic materials can be used in AM processes [41, 42]. Mainly, ceramics are cited as advanced functional materials, which enable the development of new technologies for the areas of information technology, aerospace, energy generation, bioengineering, among others. Therefore, precursor material for components with specific functions and structures in high demand [43-45].

However, certain characteristics of ceramic materials, such as high strength, make their machinability difficult, resulting in low product customization, as well as high

processing costs and long manufacturing times [46, 47]. In this sense, new forming methods are investigated to boost the production of ceramic components, where additive manufacturing is a potential technology for replacement and innovation of conventional processes [48].

In order to optimize the processing, it is commonly adopted the strategy of making the feedstock used in the AM in the form of powder/granulate, paste or in suspension, so that the layer-by-layer deposition is facilitated. In this way, during the piece manufacturing process, in addition to forming it, the material must pass to its final state, in which it will have the required physical properties or present a minimum mechanical resistance so that the constructed piece can be used in the following processing steps [34].

However, it should be noted that ceramic powders are difficult to maintain in a fine and uniform dispersion, which eventually causes sedimentation of particles during the printing process, as well as difficulty in long-term storage and poor homogeneity of the final artifact [43, 49, 50].

Based on these disadvantages, when looking for a viable alternative when in the processing route, there is an approach that brings into question the use of pre-ceramic polymers to obtain polymer-derived ceramics (PDCs), not only in terms of classic manufacturing technologies, but also in the context of AM. This is due to the fact that its processing presents greater facilities since that a polymeric precursor is used, being more easily workable, opening the range of possibilities by allowing the manufacture of the components from the use of characteristic technologies of polymers [34, 51, 52]. One of the main AM technologies used to create complex PDC-based architectures is direct-ink writing [34].

2.3.1 Direct Ink Writing (DIW)

Direct deposition of ceramic paste is arguably the most used AM technology for the generation of porous structures. The method is described as the manufacture of concentrated materials such as ceramic pastes with some organic binder. In addition, it is an easy, adaptable and low-cost technique, which can be suitable for a wide variety of materials, such as polymers, metal alloys, ceramics, as well as foods [53].

In their studies Chen et al. (2019) [54] comments that the process is based on extrusion at room temperature of non-Newtonian viscous pastes with composite rheological properties and configuration of liquid and solid phases. The viscoelastic behavior is important to ensure the production of parts that have the ability to maintain their initial shape, regardless of the action of external forces when new layers are deposited [55]. Thus, it is essential to controlling the rheological properties of the filament to prevent deformation of the part after extrusion and sagging, mainly for the cases of porous components that mostly have spanning features in its geometry. [34]

To be used, the ceramic paste must have a pseudoplastic behavior, which means, decreased viscosity when increases the shear rate, besides a high solids load, at least around >70%. The resolution for this technique is limited to filaments with a size of 100 μm [34]. In addition, the raw material must be homogeneous, without agglomerates and bubbles that make the print quality unfeasible [56].

Another recommended characteristic is the volumetric fraction between binder/additive (fillers) and ceramic powder, greater than 50%, to reduce the dimensional imprecision rate of the final product [55, 57].

The mentioned rheological properties aim to ensure the good performance of the DIW process. Since, it is understood that the precursor material must have adequate fluidity through the fine print nozzle, so that there is no clogging and self-support after the deposition process, allowing the formation of a structure without damage. Thus, meeting the requirements called extrudability and printability [47, 58-60].

2.3.2 PDC manufacturing by DIW

DIW processing can rely on different feedstocks, ranging from pure pre-ceramic polymers (PCPs) to PCP inks containing a wide variety of fillers. Processing of PCPs can occur from the liquid or molten state, which allows the adjustment of their rheological behavior and, therefore, enabling the printing of complex structures with adequate resolution and surface quality [61].

It can be seen from the research by Chen et al. [54], that complex structures of SiC ceramics were printed from using a solution of polycarbosilane in powder form and n-hexane, without addition of fillers. During the process, the concentration of

polycarbosilane in n-hexane was monitored and adjusted so that the rheological characteristics of the ink reached greater stability during the printing. The 3D scaffolds built resulted in an average porosity of 51.12 ± 2.8 vol% [60] and are represented in Figure 4.

Porosity is a characteristic considered important in the production of ceramic components. Porous and lightweight materials are interesting for numerous complex applications, such as filtration, biomedicine, catalysis, energy storage, chemical sensing, among others. These products are attractive due to their adjustable thermal, electrical and mechanical properties provided through the pore volume [62].

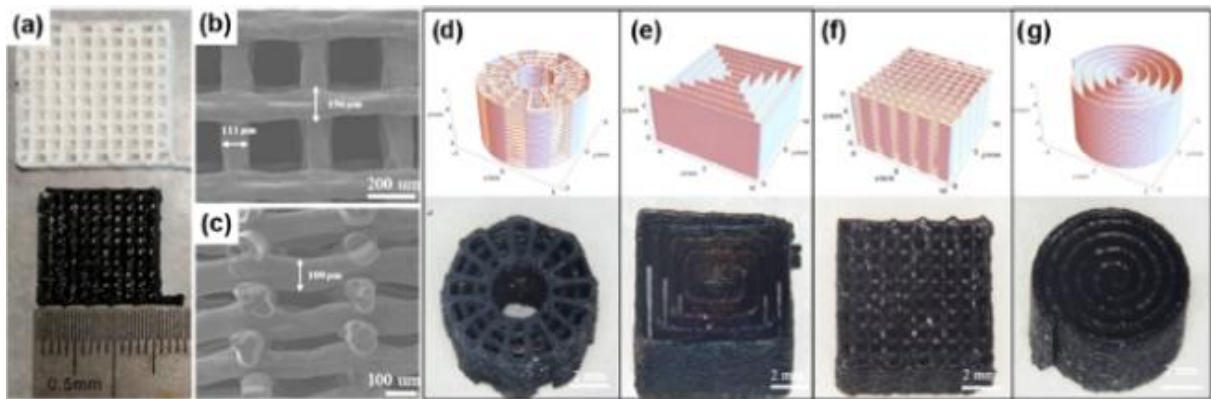


Figure 4: (a-c) Optical and SEM images of SiC 3D scaffolds (16 layers) printed with 400 μm nozzles, (d-g) 3D models and optical images of various 3D struts (32 layers) prepared through a 200 μm nozzle with polycarbosilane/n-hexane filament. Source: Adapted from [61]

In another case of application, pieces were made suitable for applications that require properties such as electrical conductivity and high thermal resistance. In this study, by Román-Manso et al. [63], such results were achieved by adding graphene oxide to polycarbosilane pre-ceramics, followed by submission to the pyrolysis reaction. In order to obtain an efficient ink release, satisfying the rheology criteria, an adaptation was carried out through a mixture of polymers, in addition to the incorporation of boron nitride particles with polysilazane to favor this control and reduce the porosity of the ceramic after the pyrolysis. Thus, showing that the desired structural and functional properties can be obtained from the addition of fillers [60].

These researches shows that the combination of direct-ink writing and PDC, allows the development of a PDC-based ink with carbon-based fillers that can be 3D printed and used as an anode for MFC.

3. AIM AND APPROACH

The aim of this research is to adapt an ink composition previously used to creating tape-casted SiOC anodes, but at this time using DIW processing. The adapted ink will be 3D printed to be later used as an anode of MFC, since the surface area and pore size higher than 1 mm, created by the 3D structure designs, combined with hydrophilicity, surface roughness and electrical conductivity, have the potential to lead to biofilm formation without pore clogging.

The chemicals content of the solid phase of the ink will be maintained constant as the previous research [16] at first, but the solid loading will be varied from 70 to 85 wt.% by reducing the solvent, p-xylene, to adapt the viscosity of the sample to the DIW process. The preceramic green bodies will be produced using a constant filament size diameter of 580 μm or tape-casted using a doctor blade with a gap of 2.0 mm. Tape-casting samples represent the starting point in means of solid loading of this research, being the standard comparison. The inks will be pre-tested by simulating a printing process using a syringe and analysed by shear rate rap rheological test in a rotational rheometer.

Once a suitable ink viscosity is found, printing parameters such as nozzle size of 580 μm and speed of 10 mm/s will remain constant, varying the deposition pressure and the geometry of the 3D structure between lattice cuboids and cyllindroids, while the infill between rectilinear and honeycomb. After 3D printing, drying will be carried under room temperature for 24 hours followed by a pyrolysis reaction at 1000°C under nitrogen atmosphere in order to achieve a hydrophilic behavior.

The effect of the manufacturing process on the resulting surface structure will be characterized through scanning electron microscopy to verify images of the top surface, cross section and layer-by-layer views of the samples. The pore structure will be evaluated through the mercury intrusion porosimetry to measure the pore size and the open porosity, and nitrogen adsorption by using BET method to assess the specific surface area.

Later, the functional properties will be analysed by vapor adsorption, using water and n-heptane to assess the hydrophilicity; the electrochemical impedance spectroscopy to verify the electrical conductivity; and the chemical stability to check the weight variation of the samples over time.

4. MATERIALS AND METHODS

4.1 Sample Preparation

Due to a successful application of SiOC tapes as anodes in MFC [16], the composition of the solid phase from this previous published work was used in this work. The final objective is to keep the solid phase composition fixed and reach an optimal solid loading to the 3D printing process. The components of the solid phase, their wt.% in the solid phase and their function are described below in Table 2. The solid loading varies from 70 to 85 wt.% by varying the solvent p-xylene.

Table 2: Weight fraction of each component in solid phase. Source: Adapted from [16]

Material	wt.%	Function
Methyl silsesquioxane (Silres ® MK pulver – Wacker)	20	Preceramic precursor
Methyl phenyl silsesquioxane (Silres ® H44 pulver – Wacker)	20	Preceramic precursor
Molybdenum disilicide MoSi ₂ Grade A (AB 134570 – abcr)	8	Control shrinkage
Azodicarbonamide 97% (A96606 – Sigma Aldrich)	17	Pore formation inducer
Carbon Black (Vulcan XC72 GP-3907 – Cabot)	5	Conductive filler
Graphite (timrex KS75 P-233D – Timcal)	29.2	Conductive filler
Imidazole 99% C ₃ H ₄ N ₂ (A10221 – Alfa aesar)	0.8	Cross-linking agent

Prior to the mixing process, the solid phase, except for the imidazole, was ball milled for 24 hours under a velocity of 90 rpm to ensure later an easier mixing of the solid phase with the liquid phase, the p-xylene as an organic solvent. The volume proportion of solid phase, milling balls and empty space in the recipient was of 1:1:1. The milling balls used were composed of alumina and with a diameter size of 9.70 ± 2.0 mm. The inks were prepared at room temperature using magnetic stirrer for inks with solid loading up to 80 wt.% or a mechanical stirrer for ink with 85 wt.%. After 30 minutes of mixing under room temperature, cross-linking agent, Imidazole, was added while stirring continuously for more 30 minutes. Figure 5 shows the processing route.

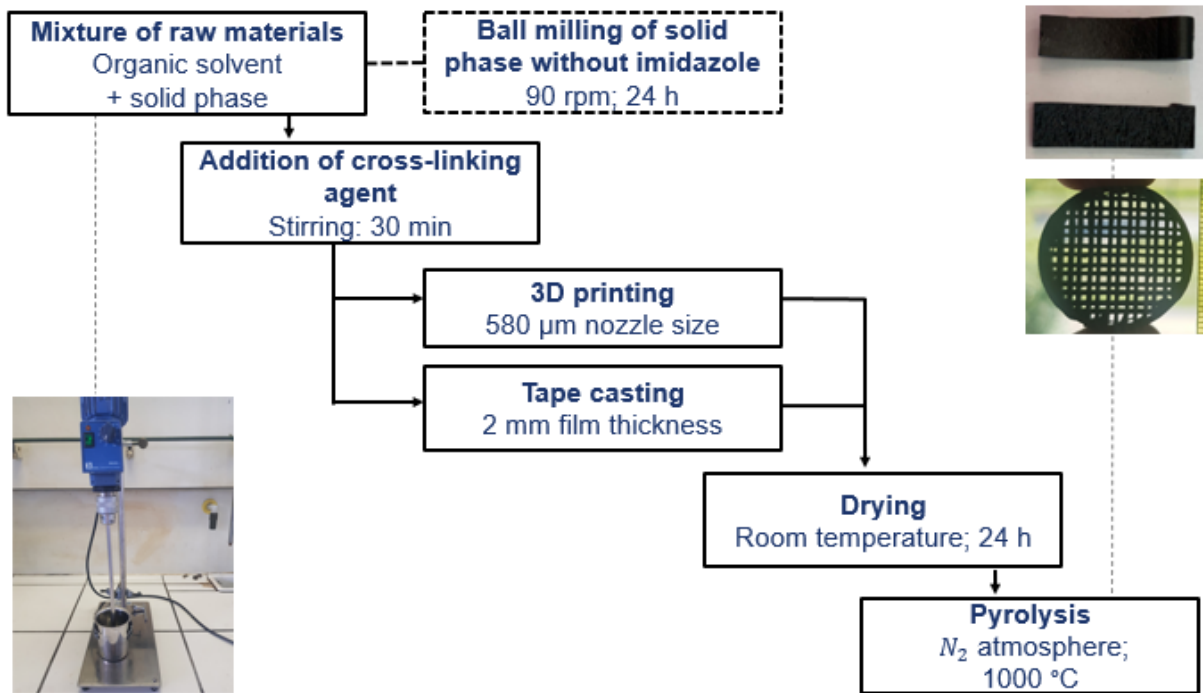


Figure 5: Diagram of the sample's preparation step by step, using both processing routes, 3D printing and tape-casting. Source: Author.

During mixing procedure, solid loading of the ink was controlled by weighting the ink mass and adding or removing solvent. After complete mixing, one portion of the developed ink was used in rheological tests and the rest of the prepared ink was processed by 3D printing or using tape-casting processing route. To 3D printing the samples was used the 3D printer Cellink INKREDIBLE® 3D in lattice cuboid or lattice cylindroid geometry, using nozzle diameter of 580 μm and velocity of 10 mm/s. To tape-casting the samples was used the Doctor Blade at 2 mm of thickness. After printed or tape-casted, the samples were dried at room temperature for 24 hours. Later, the cross-linked and dried samples were pyrolyzed at 1000°C under nitrogen atmosphere to convert them into ceramic material.

4.1.1 Samples Labeling

To organize the developed samples and their results, a labeling system was created to identify the varied parameters. Thus, the first term represents the processing route, the second term is the solid loading and the third term is in reference of the content of azodicarbonamide. As an example, a composition named as 3D - 85 wt.% - Azo 17%, represents a 3D structure with solid loading of 85 wt.% and 17 wt.% of

azodicarbonamide. Figure 6 describes all three terms and their variables investigated in this work.

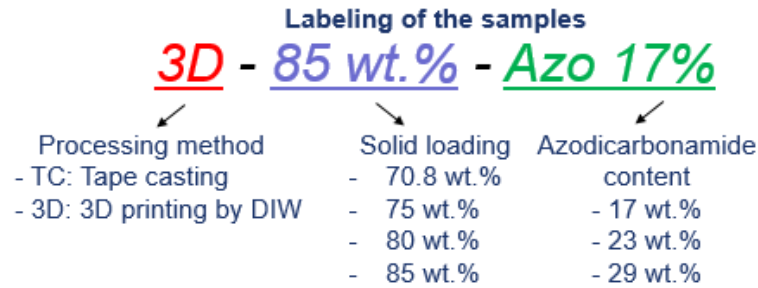


Figure 6: Labeling system of the samples analysed in this work, presenting the three terms that define them and their modifications studied respectively. Source: Author.

4.2 Analysis and Measurements

The analysis were done before and after the pyrolysis reaction. Table 3 below depicts the analysis and its purpose.

Table 3: Analysis and measurements to evaluate the samples and its purpose. Source: Author.

Step	Analyse	Purpose
Before pyrolysis	Syringe test	Ink potential for 3D printing
	Rheology behavior	Yield point of the ink
After pyrolysis	SEM images	Surface structure of the filament
	Hg intrusion porosimetry	Pore window size and open porosity
	Nitrogen adsorption	Specific surface area
	Vapor adsorption	Hydrophilicity
	Electrochemical impedance spectroscopy	Electrical conductivity
	Chemical stability	Weight loss over time

4.2.1 Rheology behavior

A portion of the ink was separated after mixing, for rheological test, to assess the yield point to later correlate the success of the 3D printing with the solid loading used. The rheological characterization was made with the rotational rheometer

Malvern Kinexus Pro+®, at room temperature, 25 °C. A plate-plate were used as testing geometry. Figure 7 shows a scheme of the rotational rheometer technique.

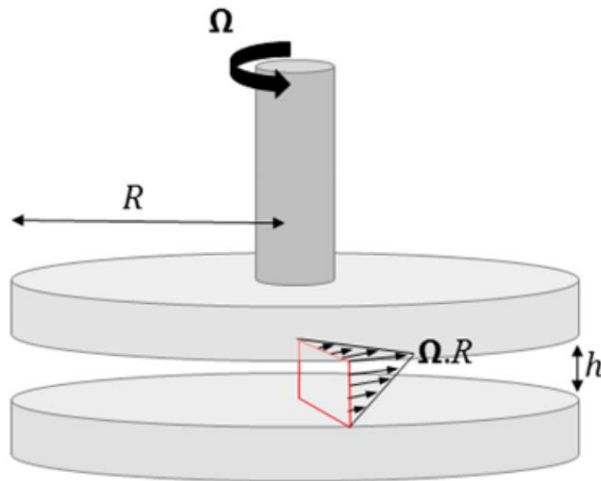


Figure 7: Scheme of the rotational rheometer technique used with plate-plate geometries. Source: [64].

The type of test performed was a shear rate ramp test, with a continuously increase of the applied shear rate from 0.1 to 1000 s^{-1} . As a result, shear viscosity versus shear stress curves were obtained and yield point of the ink can be identified as the point where shear viscosity value drops steeply. Identical tests were performed with the same inks 3 times to assure more confident results.

Figure 8 depicts the graph representation of the yield point, defined as a dynamic test to simulate the flow initiation.

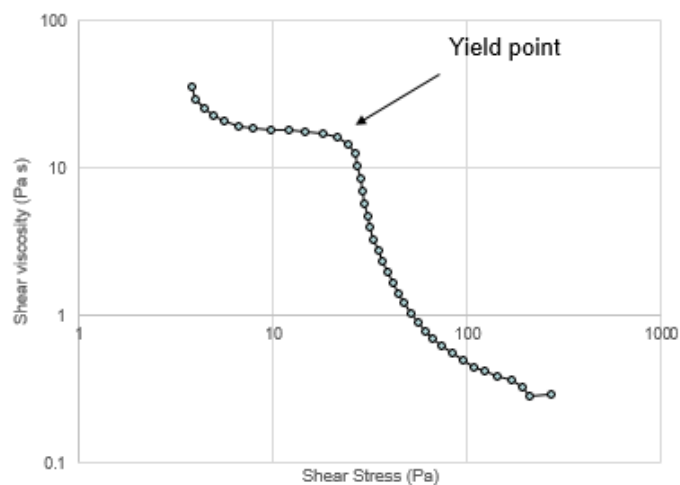


Figure 8: Graph representation of the yield point. Source: Author.

4.2.2 Scanning Electron Microscope

The SEM instrument is based on the principle that the primary electrons released from the source provide energy to the atomic electrons of the specimen which can then release as many signals like the secondary electrons (SEs). An image can be formed by collecting these secondary electrons from each point of the specimen. The basic requirement for SEM is to operate under vacuum to avoid interactions of electrons with gas molecules in order to obtain images with high resolution. [65]

The SEM Camscan Series 2, Obducat CamScan Ltd., Germany was used to analyse the pore morphology; using BSE electrons and magnifications of 500× and 2000× producing images with scales of 50 μm and 10 μm, respectively. Prior to measurements, samples were sputtered with gold with K550, Emitech, Judges Scientific plc. UK. The cross-section and top view of the filaments successfully 3D printed ink (only with 85 wt.%) was analysed for better understanding the influence of the processing technique, solid loading and azodicarbonamide content on the formation of the pore structure.

4.2.3 Mercury Intrusion Porosimetry

The mercury (Hg) intrusion analysis is a technique used to analyse many pore structure parameters like the pore window size distribution and the open porosity. The analysis starts with drying the specimen to empty the pores from any existing fluid, and then weighed, following by transfer the sample to a chamber, which is evacuated, and mercury is introduced into the specimen with the help of external pressure.

Pressure in progressive increments is applied to the mercury and the pressure used at each step is monitored. The set of pressure steps and corresponding volumes intruded provides the basic data for pore size distribution calculations.

The Washburn equation may be properly applied to estimate the diameter of the capillaries intruded at each pressuring step [66],

$$d = \frac{-4\gamma \cos\theta}{P} \quad (\text{Equation 3})$$

Where d is the diameter of the capillaries being intruded, γ is the surface tension of mercury, θ is the contact angle of mercury on the solid, and P is the applied pressure.

To analyse each SiOC samples were used three pieces of 0.5 cm², without any pre-treatment, characterized by Mercury Porosimeter Pascal 140 and 440, POROTEC GmbH, Germany, assuming cylindric pores model and a contact angle of 141° to calculate the results.

4.2.4 Nitrogen Adsorption

This analysis is given by the adsorption and desorption of nitrogen gas on a solid surface at 77K. From this process, the data are plotted on a graph with the adsorbed volume of nitrogen at 273.15 K and 101.3 kPa by the equilibrium relative pressure given by p/p_0 , where p_0 is the nitrogen vapor pressure at 77 K. [67]

The different types of isotherms are characteristic of different types of porous materials, according to the International Union of Pure and Applied Chemistry (IUPAC) definition, there are 6 isotherms types [68].

Type I characterizes microporous solids with small external surfaces. Type II, non-porous or macroporous adsorbent. Type III is convex to the p/p_0 axis over its entire range, this type is not common. Type IV, mesoporous adsorbents, the initial part is similar to type II, being attributed to monolayer-multilayer adsorption. Type V, weaker adsorbent-adsorbate interaction, is uncommon. Lastly, type VI, non-porous surface, under multilayer adsorption [67]. All types are presented in Figure 9.

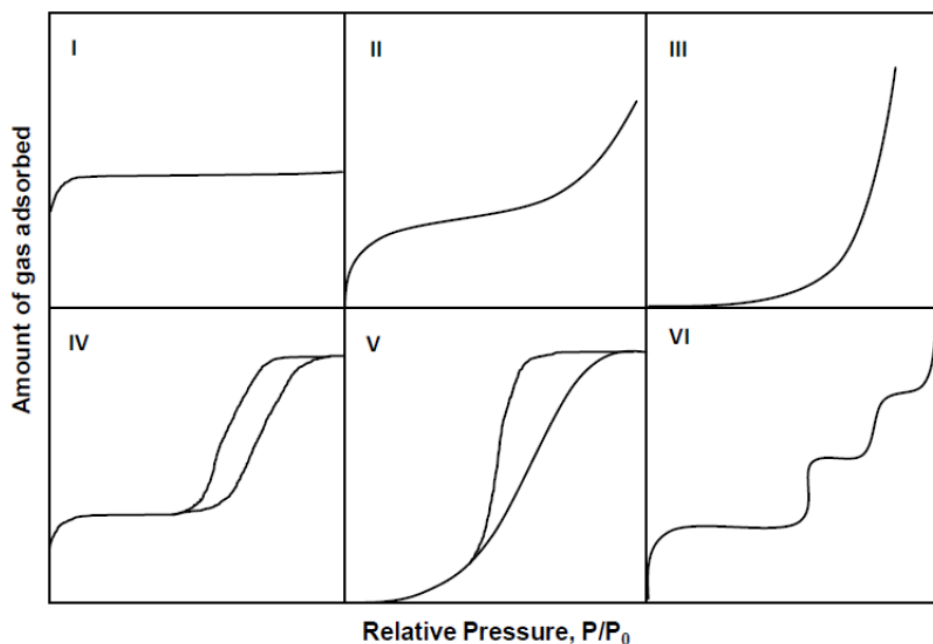


Figure 9: Isotherms classification by IUPAC. Source: [68].

The adsorption of nitrogen gas was recorded in relative pressure range from 0.05 to 0.995. From isotherm data, the determination of specific surface area was calculated by Brunauer-Emmett-Teller (BET) method [69]. Prior to measurement, about 0,2 grams of the samples were hand-milled into powder and sieved using a sieve with 300 mesh.

Later, the powder was placed in the sampling glass and a pre-treatment step was done at 120 °C for 3 hours to eliminate any remaining humidity from the powder. Lastly, the sampling glass was purged with argon for 30 minutes at room temperature. The nitrogen adsorption isotherms were measured using BELSORP-mini, BEL Japan Inc [70].

4.2.5 Vapor Adsorption

Materials, when present in the environment, can relate to it in different ways, in which different functional groups or even their absence can define how their surface chemical interaction will be. Therefore, to determine the hydrophilic or hydrophobic behavior according to the interest of this work, the interaction of the samples with the solvents water and n-heptane was adopted, being polar and non-polar respectively [71].

From the measurement of the dry sample weight and after a period of adsorption under ideal pressure conditions at separated flasks, it is possible to provide relevant data in determining the hydrophilic or hydrophobic behavior of the samples. By analyzing the weight of the adsorbate with both solvents you can determine which one had the greatest interaction. The greater the adsorption with the polar solvent, water, the greater the hydrophilic behavior and, on the other hand, the greater the adsorption with the nonpolar solvent, n-heptane, the greater the hydrophobic behavior [72].

All measurements were performed in triplicate to assure reproducible values. The samples were ground until a maximum granulometry of 300 mesh was obtained, and then about 0.5 g were weighed in 15 ml flasks placed in an oven at 70°C for 24 hours to remove any moisture and other organic solvents still present. Then, the flasks were placed in the desiccator for 30 minutes and weighed again, obtaining the dry weight of the samples. Subsequently, each flask was placed individually and opened in a closed Erlenmeyer containing water or n-heptane for a period of 24 h.

In each Erlenmeyer, the liquid solvent was in equilibrium with its vapor phase at ambient conditions, at 20°C and 1 atm. At the end of these 24 hours of adsorption, the flasks were weighed again to obtain the adsorbed weight. Finally, to determine whether the surface had hydrophilic or hydrophobic characteristics, was calculated the difference between the adsorbed weight and the dry weight of the sample to check if the adsorbate weight was higher in water or n-heptane and then, with the values of specific surface area from BET, was calculated the adsorbed vapor mass per unit of area and per unit of mol using molar mass of which solvent. The final result is the ratio between the adsorbed vapor mass of water by adsorbed vapor mass of n-heptane.

4.2.6 Electrochemical Impedance Spectroscopy

It is usually characterized by the process of applying an alternating current, the result of a sinusoidal potential excitation, in a given material, in which the current flowing through the material will then be measured in order to verify the difficulty that the current faces when crossing the material, which is called resistance.

This method is quite versatile, being able to characterize many of the electrical properties of materials and their interfaces with electrodes. Different cases, such as corrosion processes, fuel cells, among others, can be analyzed as the dynamics of loads can be investigated in any type of material, regardless of whether it is ionic, semiconductor, mixed electronic-ionic or even dielectric [73, 74].

For this work, the electrical conductivity of the samples was explored from the EIS analysis. The equipment used was the Impedance Measurement Unit IM6ex Zahner Electric with THALES software. The parameters were defined to a voltage at 0.7 volts, an alternating current amplitude of 10 mV covering a frequency range from 10 mHz to 1 MHz in a decreasing way, followed by the increasing path.

The measurement was done at room temperature, with a rectangular shaped sample, in which the approximate dimensions were 17.5 ± 2.5 mm in length by 7.5 ± 0.5 mm in width, and the samples processed by tape-casting were 2.0 ± 0.3 mm thick while those processed by 3D printing 3.2 ± 0.3 mm. Figure 10 show the sample and contact configuration to the measurement.

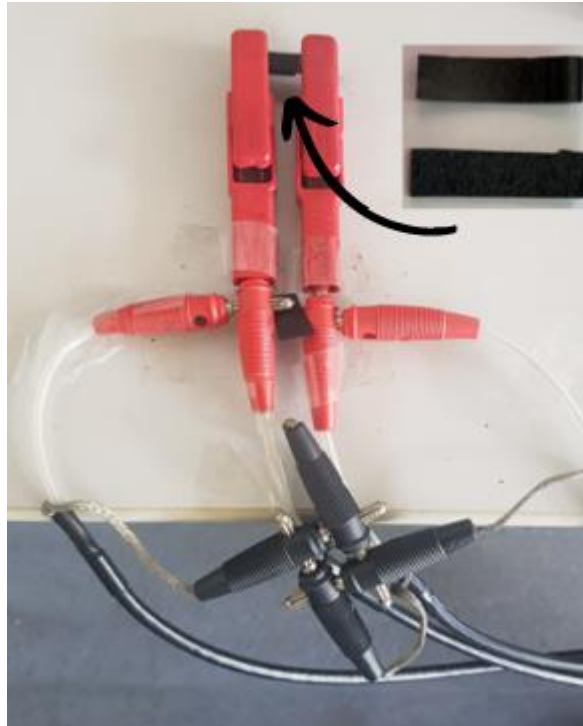


Figure 10: The sample shape on right side and the contacted configuration during EIS measurement.

Source: Author.

The second Ohm's law equation was used to calculate the electrical resistivity of the sample and then the inverse of the result was calculated to obtain the thermal conductivity values.

$$\rho = \frac{R \cdot A}{L} \quad (\text{Equation 4})$$

Where ρ is the electrical resistivity of the sample, R is the resistivity measured from the EIS, A is the area of the rectangular sample, and L is the length of the sample.

4.2.7 Chemical Stability

As the material developed in this work has applications in which it will be exposed in a chemically harsh environment when being in direct contact with wastewater during its use, the decomposing rate of the material becomes a very important factor to be observed, since the prolonged time can lead to deterioration and destruction of the material. In this environment, the corrosion that occurs is electrochemical, represented by the reactions at both chambers, the anode and the cathode [75, 76].

The materials most commonly used for this application are graphite felts, which are quite susceptible to electrochemical oxidation, therefore, the use of ceramic materials is totally positive in terms of preserving their chemical stability and minimizing the impacts of corrosion [75, 76].

To assess the corrosion rate, a possibility is to simulate the application conditions in which the material will be exposed and then measure by the gravimetric method. Thus, parameters such as temperature and average pH of the environment were preserved, using the phosphate buffer solution (PBS) at 20 °C and pH 7.

For this, the samples were previously placed in an oven at 70°C for 24 h and weighed to obtain their initial weight. After that, 20 ml of the PBS solution was placed in 45 ml vial, each sample was inserted in a different vial and then the vials were closed. Thus, the sample was kept in this condition for a period of 4 weeks, and each week the samples were weighed to be able to follow the evolution of the corrosion rate weekly.

Every 7 days the samples were removed from the vials, rinsed with distilled water to remove any traces of the PBS solution and prevent the continuation of corrosion in certain regions, placed in an oven at 70°C for 24 h to dry and weighed again. After that, a new PBS solution was prepared so that the sample was immersed in the vials again and remained until the complete period was completed.

5. RESULTS AND DISCUSSION

5.1 3D Printing Optimization

The 3D printing optimization represents if the filaments can maintain its shape after printed. This characteristic was assessed through the results from the syringe and rheological tests. Therefore, prior 3D printing, all inks compositions with solid loading ranging from 70 to 85 wt.% were manually extruded using a syringe to preliminarily verify if the filaments extruded could sustain its shape, not sag or deform over time or after the addition of weight from subsequent filaments layers deposition.

Furthermore, the shear rate ramps, assessed through shear viscosity versus shear stress, allows to determine the yield point. This dynamic test allows to simulate the flow initiation behavior of the ink, which is an important measure to analyse the release of the ink through the nozzle when printing.

Figure 11 indicates that the ink's composition with solid loading of 70 and 75 wt.% are not suitable for 3D printing as the filaments even in the first layer are not stable. Although the ink with 70 wt.% of solid loading were successfully used in previous work for the tape-casting processing [16], in this work the same solid loading proved to be unfeasible for the 3D printing route as a stacking of layers is not possible.

The rheology measurements indicate a yield point of the ink with solid loading of 70 and 75 wt.% of $25,87 \pm 2,24$ Pa and $83,12 \pm 1,89$ Pa, respectively, both are presented in Figure 12, which their curves are defined. Results from rheology measurements are summarized in Table 4.

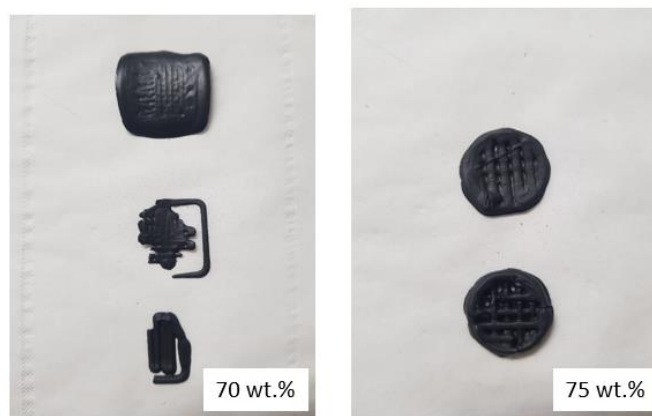


Figure 11: Left) Three 3D samples using solid loading of 70 wt.% and lattice cuboid geometry. Right) 3D printing samples using solid loading of 75 wt.% and lattice cylindroid geometry.

Source: Author.

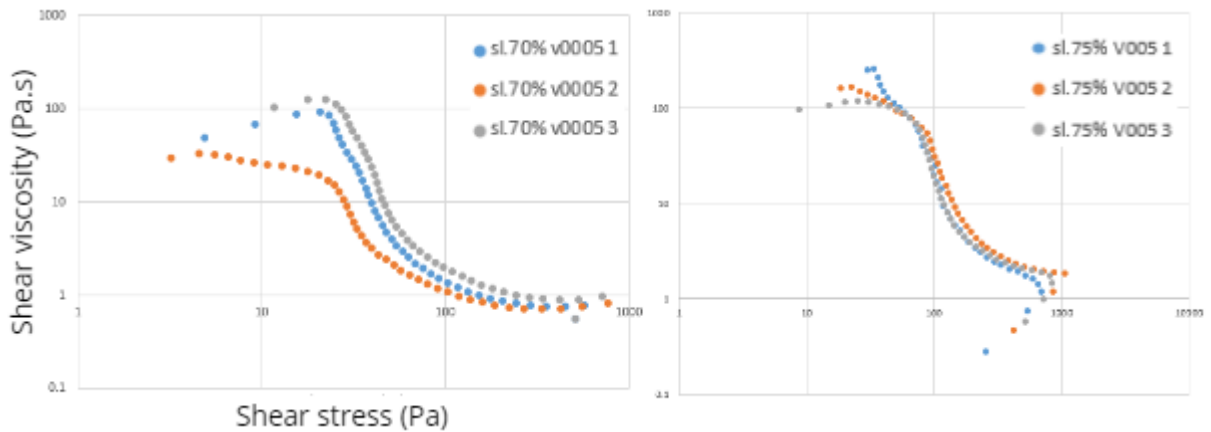


Figure 12: Left) Rheological behavior curve using solid loading of 70 wt.% and shear rate ramp test. Right) Rheological behavior curve using solid loading of 75 wt.% and shear rate ramp test. Source: Author.

Table 4: Yield points of different solids loading from shear stress ramp rheological test. Source: Author.

Sample	Yield point (Pa)
3D - 70% - Azo 17%	$25,87 \pm 2,24$
3D - 75% - Azo 17%	$83,12 \pm 1,89$
3D - 80% - Azo 17%	197.13 ± 6.54
3D - 85% - Azo 17%	1141.33 ± 32.33

On the other hand, when increasing the solid loading of inks to 80 wt.%, preliminary syringe tests indicate in a first moment a possible printability and also an increase of the yield point to 197.13 ± 6.54 Pa, as shown Figure 13. Nevertheless, when 3D printing this solid loading, the filaments were not stable during subsequent printing of other layers and collapsed on its base. Both cases are presented in Figure 14.

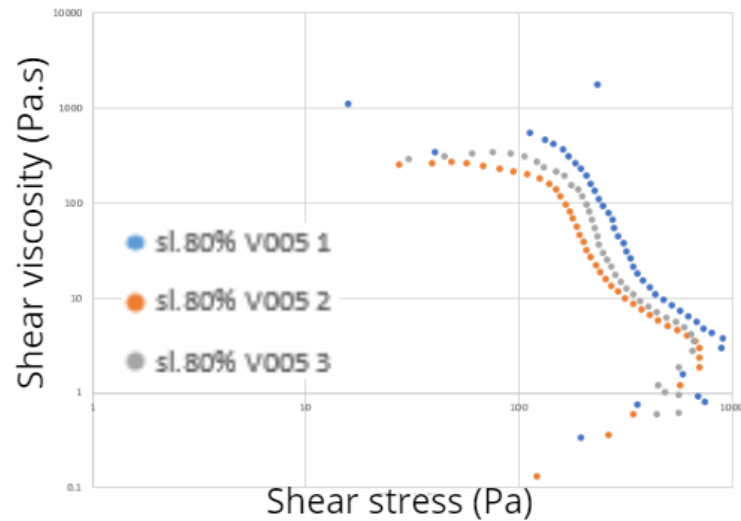


Figure 13: Rheological behavior curve using solid loading of 80 wt.% and shear rate ramp test.

Source: Author.

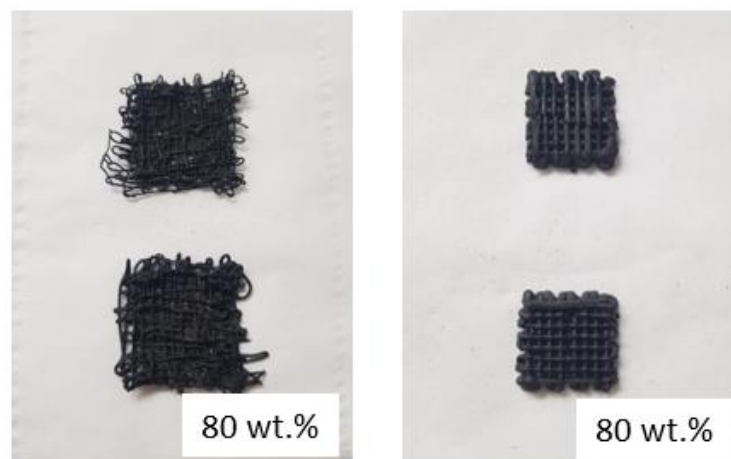


Figure 14: Left) Syringe test using solid loading of 80 wt.%. Right) 3D printed samples with the same loading. Source: Author.

Lastly, all the filaments printed using the ink with 85 wt.% of solid loading were stable during the whole printing program, as shown Figure 15. The yield point of the ink increased steeply to 1141.33 ± 32.33 Pa, depicted in Figure 16, demonstrating that the yield point increases exponentially with the solid loading, as Table 4 presented above.

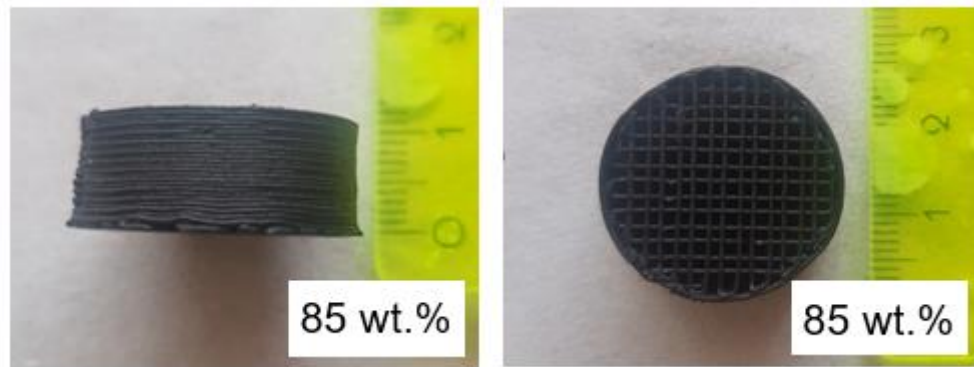


Figure 15: Left) 3D printing using solid loading of 85 wt.% showing the layer-by-layer of a lattice cylindroid geometry. Right) 3D printing using solid loading of 85 wt.% of the same sample, but showing the top view and its infill. Source: Author.

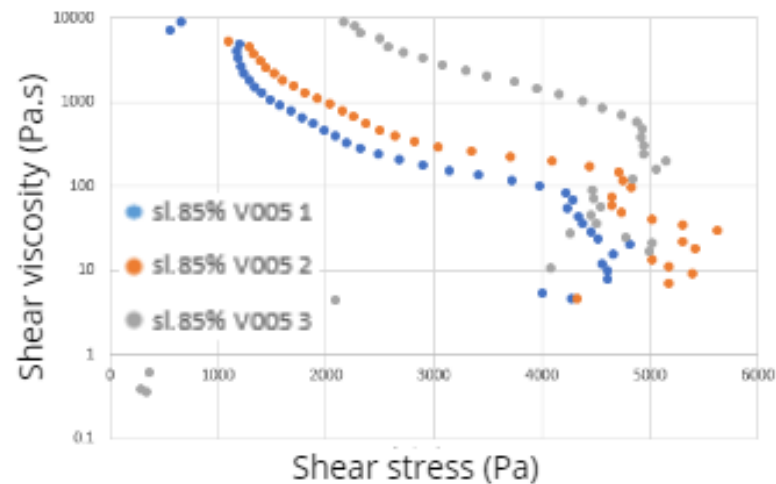


Figure 16: Rheological behavior curve using solid loading of 85 wt.% and shear rate ramp test. Source: Author.

As the ink with 85 wt.% of solid loading was the only one stable during 3D printing process, the subsequent analysis of the pore structure and functional properties, performed after pyrolysis, were made for this composition, varying only the processing route, being through tape-casting or DIW; and the AZO content from 17 to 23 and 29 wt.%.

5.2 Surface Structure

The surface structure of the pyrolyzed material can indicate, by means of roughness, if bacteria adhesion can be successful when the material is applied as anode. The analysis of the surface structure was done through the results from SEM

images. Firstly, an overview of the pore structure was done, on the top surface and cross-section views of the tapes and filaments, besides the layer-by-layer view of the filaments.

For this analysis, the aim was to qualitatively verify the surface roughness and distribution along the thickness of each sample, depending on the process route used. Additionally, it was also investigated how the increase in the amount of AZO to 23 and 29 wt.%, could influence on the formation of pores on the surface of the 3D printed samples. As the AZO is a pore formation agent, a surface with more pores was expected as the percentage of AZO was increased, the results of the SEM images are present in Figure 17.

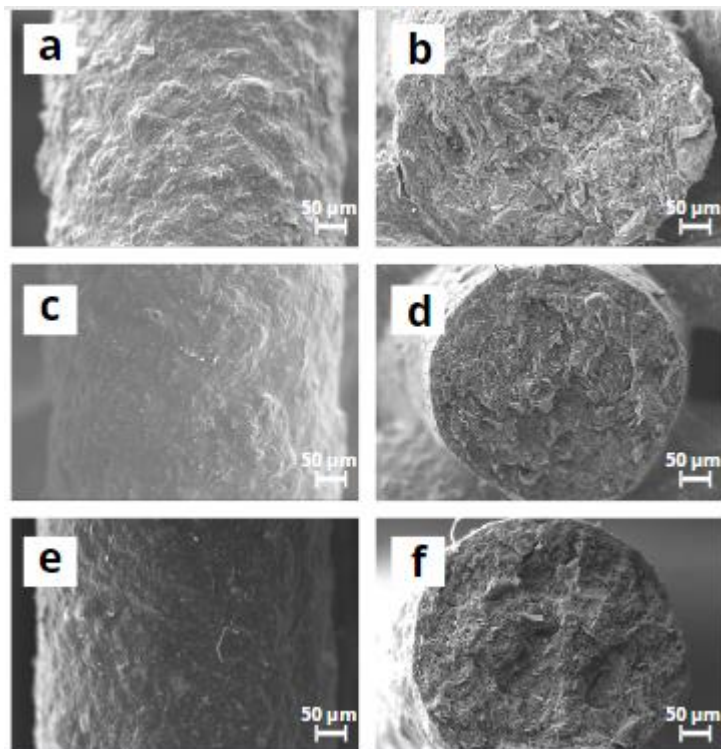


Figure 17: Different views of 3D structure using AZO at 17, 23 and 29 wt.%. a) surface view in 500x magnification of AZO at 17%; b) cross-section view in 500x magnification of AZO at 17%; c) surface view in 500x magnification of AZO at 23%; d) cross-section view in 500x magnification of AZO at 23%; e) surface view in 500x magnification of AZO at 29%; f) cross-section view in 500x magnification of AZO at 29%. Source: Author.

The images show that the increase in the number of pores on the surface of the filaments did not occur as the expected, which may have been due to the high solid loading of the ink's composition, necessary to maintain the 3D structures stables. Therefore, increasing AZO at the expense of decreasing graphite in order to facilitate

biofilm formation should be evaluate by verifying the following analysis to assess further information and properties concerning about the pore structure.

Overall, the SEM images indicate qualitatively a certain surface roughness on the filaments or tapes at higher solid loadings as 85 wt.%, which can be beneficial for the biofilm adhesion. Alternatively, the surface of the tapes with 70.8 wt.% showed a much less rough surface, as shown in Figure 18. This can also be noted when comparing the image of the top surface of the tape-casted sample using 85 wt.% and the 3D printed with the same solid loading, demonstrating similarities in terms of roughness.

Surface defects, as cracks are not visible in any sample, indicating a mechanical stability even after contractions during the pyrolysis at 1000°C. Figure 19 shows that the layer-by-layer deposition was successful, showing perfect match between each filament and indicating that the printing parameters such as printing velocity and pressure were successfully optimized.

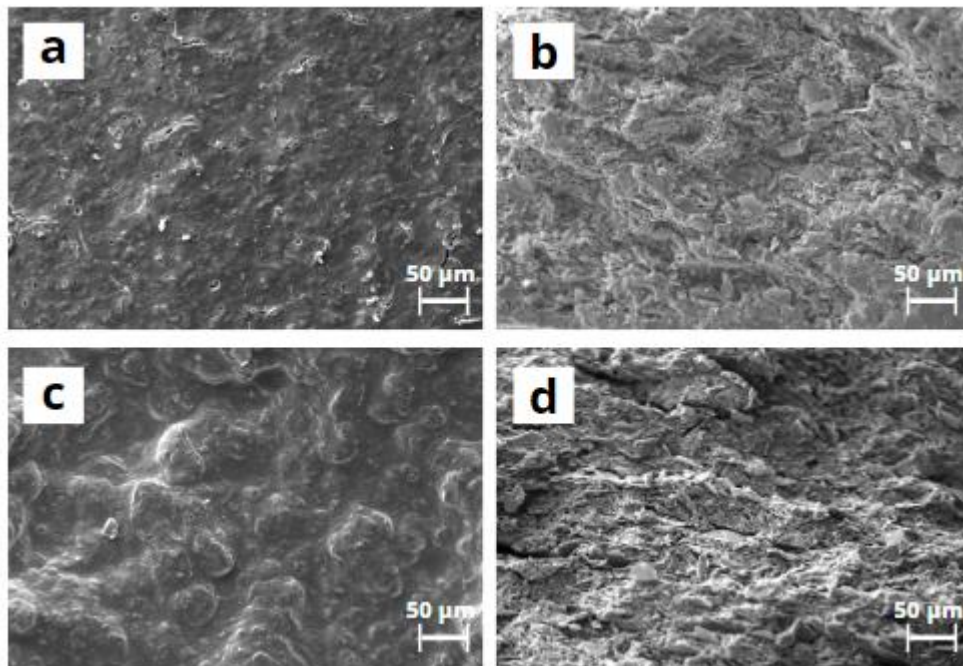


Figure 18: Different views of tape-casting structure using 70.8 and 85 wt.%. a) surface view in 500x magnification of 70.8%; b) cross-section view in 500x magnification of 70.8%; c) surface view in 500x magnification of 85%; and d) cross-section view in 500x magnification of 85%. Source: Author.

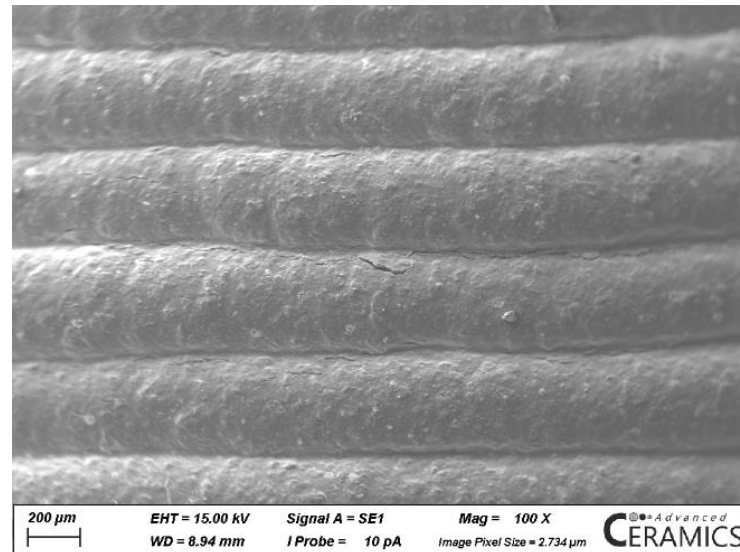


Figure 19: Layer-by-layer view of the 3D structure with 85 wt.%. Source: Author.

5.3 Pore Structure

The pore structure of the pyrolyzed material can indicate, by means of pore size on surface and specific surface area, if the biofilm formation can be successful when the material is applied as anode. The analysis of the pore structure was done through the results from two different analysis, the mercury intrusion porosimetry and nitrogen adsorption by using the BET method.

The results of the Hg intrusion porosimetry analysis are depicted in Figure 20, in addition to the summarized values of average pore window size and open porosity presented in Table 5. On one hand, the average of pore window size distribution values ranges from 0.21 to 105.50 μm , not varying significantly by changing the processing route. On the other hand, an increase of the solid loading led to a high decrease of the average pore window size, representing a higher compacting of the solid phase components. Although the pore sizes are mostly in the macropore range (>50 nm), it is also possible to note a smaller number in the mesopore range, between 2 nm and 50 nm, in all samples.

The higher volume of macropores can be explained by the collapse of the micro and mesopores during the pyrolysis above at 500°C. Although the pore size on the surface of filaments is small for the 85 wt.% samples, biofilm clogging may be avoided by the infill between the filaments of the designed 3D structure.

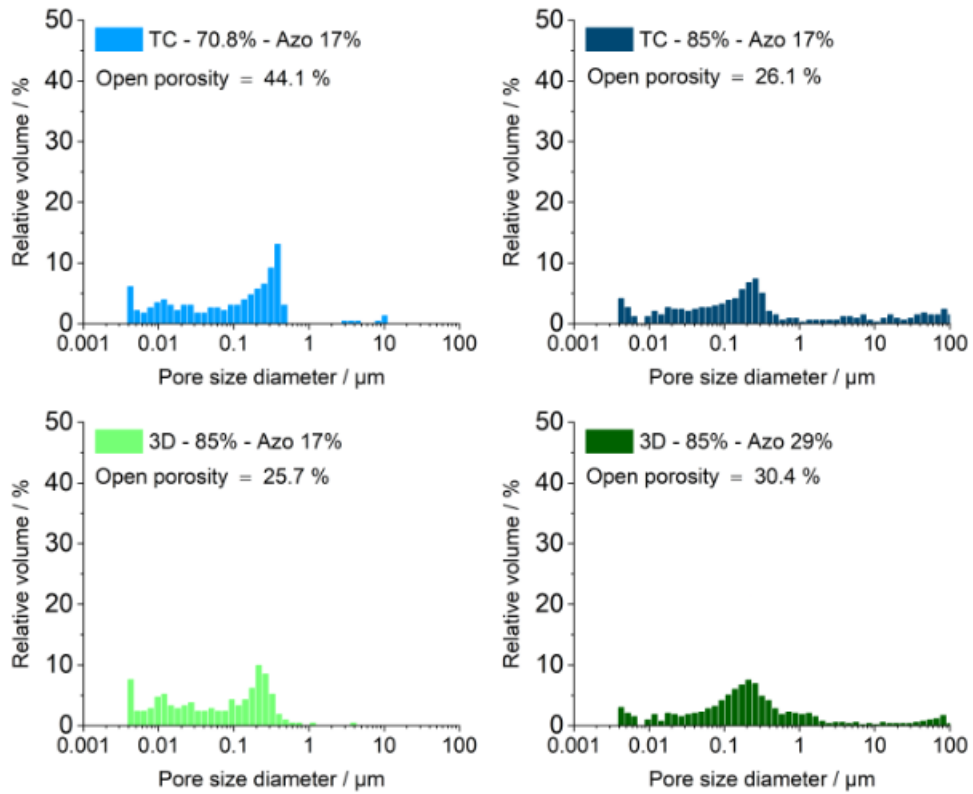


Figure 20: Pore window size distribution and open porosity from Hg intrusion porosimetry. Source: Author.

The open porosity ranges from around 25 to 44% depending on the AZO amount and the solid loading used. The increase in the AZO content to 29%, increases the open porosity by 5%. An increase of the solid loading decreases the open porosity from 44.02 to 26.31%, independently of the processing method. Nevertheless, an increase of the solid loading may lead to an increase of the electrical conductivity due to an increase of the wt.% of carbon-based fillers in the composition.

Table 5: Average pore window size and open porosity from Hg intrusion porosimetry. Source: Author.

Sample	Average pore window size (μm)	Open porosity (%)
TC - 70.8% - Azo 17%	105.50	44.0
TC - 85% - Azo 17%	0.26	26.3
3D - 85% - Azo 17%	0.21	25.7
3D - 85% - Azo 29%	0.21	32.0

The nitrogen adsorption analysis through the BET method, indicates specific surface area varying from 21.95 to 82,51 m^2/g , shown in Figure 21, mainly influenced by the processing route and the AZO content. Against the expected, using the same composition, varying only the route from tape-casting to 3D printing, an increase around 2.5 times was noticed. The variation was actually expected by varying the solid loading, although, by analysing the samples TC - 70.8% - Azo 17% and TC - 85% - Azo 17%, both samples presented the same result, which did not follow the trend.

On the other hand, increasing the AZO content from 17 to 29 wt.% decreases the specific surface area around 0.75 times, from 82,51 to 21.95 m^2/g . Regarding this, the decrease of the specific surface area can be attributed to a lower amount of the carbon-based fillers in the composition.

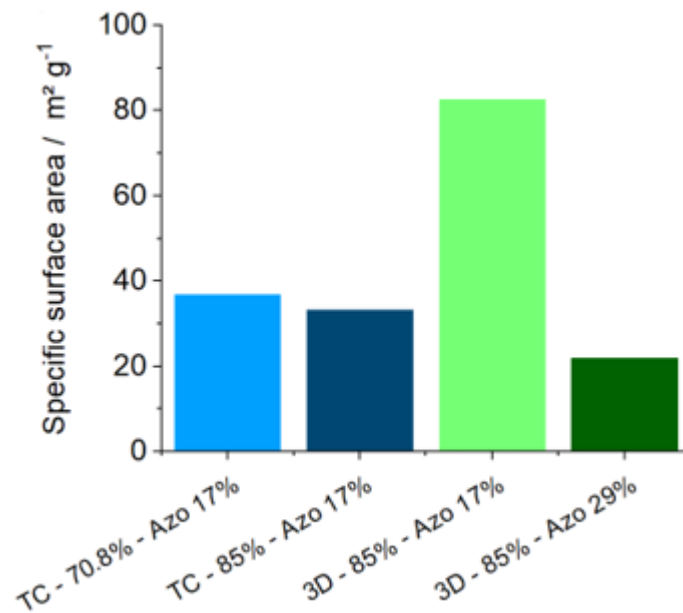


Figure 21: Specific surface area of the samples from BET method. Source: Author.

Figure 22 shows the adsorption isotherms of the samples, indicating an isotherm type IV that associates materials that endow mesoporosity, in addition to show that the higher the adsorbed volume is, the higher the specific surface area. For PDC-based materials pyrolyzed at 1000°C the specific surface area of the samples, especially the 82,51 m^2/g are high, as verified when comparing not only with the previous research [13, 16], but between the others samples of this work. This increase of the specific surface area may be associated with a higher amount of carbon black in the composition, which shows a specific surface area of 44.8 m^2/g as a pure filler.

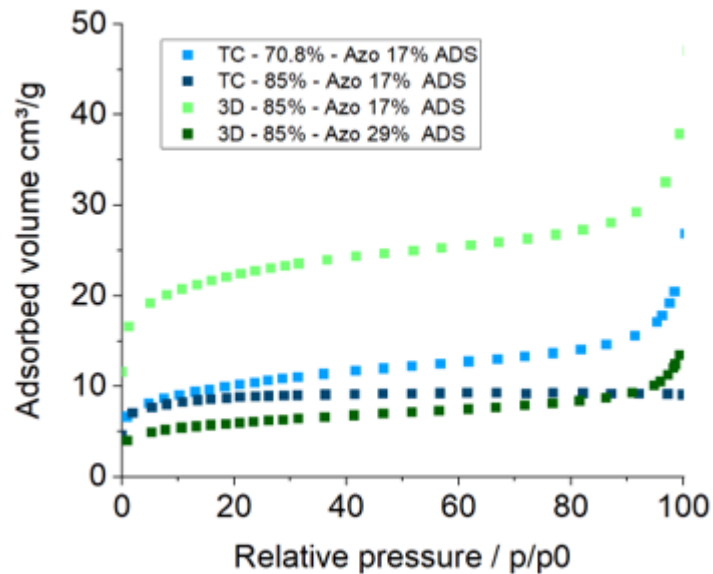


Figure 22: Nitrogen adsorption/desorption isotherms of the samples. Source: Author.

5.4 Functional properties

Some functional properties were evaluated in this work to obtain indicatives of the performance of the material when applied as an anode to MFCs. For this, data were collected from three different analysis, which were vapor adsorption, electrochemical impedance spectroscopy and chemical stability.

The results of vapor adsorption served to define the hydrophilic behavior of the samples. Since all samples were pyrolyzed at 1000°C, a hydrophilic behavior was expected for all of them. From the analysis of the Figure 23, it can be inferred that, as expected, all samples present a ratio of the water by n-heptane greater than 1, which means that all of them present hydrophilic behavior. The hydrophilicity property is very important regarding to the bacteria interacting, enabling their adhesion and the biofilm formation on the anode.

The ratio ranged from 5.0 to 6.2, mostly influenced by the solid loading and the AZO content. When using different solid loadings, evidenced by samples TC - 70.8% - Azo 17% and TC - 85% - Azo 17%, respectively, a decrease of 1 point was observed, which can be explained according to the lower open porosity on surface when using higher solid loading, as shown previously in Figure 20. Following the same idea, this same explanation can be used to justify the ratio 1.1 points higher when comparing the

samples 3D - 85% - Azo 17% and 3D - 85% - Azo 29%. The increase of the AZO content from 17 to 29 wt.% promoted better hydrophilic behavior.

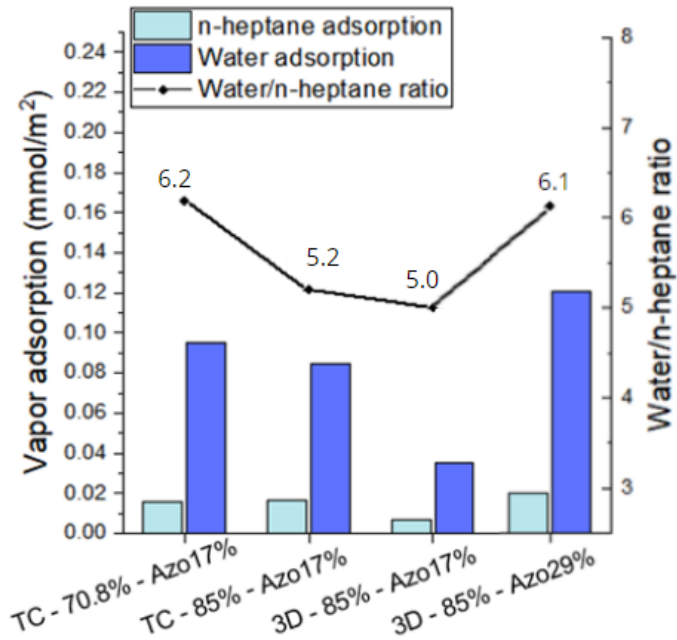


Figure 23: Vapor adsorption by water and n-heptane solvents and its ratio. Source: Author.

The electrical conductivity was evaluated by the electrochemical impedance spectroscopy, in which rectangle samples with 17.5*7.5*2.0 mm in length, width and thickness, respectively, were cut from the tape-casting route and 3D printed using 17.5*7.5*3.2 mm measurements. The results are depicted in Figure 24 and Table 6, varying from 0.57 to 1.89 S/m, show that using the same composition, when only modifying the processing route from tape-casting to DIW, referred by samples TC - 85% - Azo 17% and 3D - 85% - Azo 17% respectively, led to values around 1.5 times higher, the better conductivity of the 3D printed sample can be partially explained by the winding way in which the material was deposited during 3D printing.

To the 3D printed sample another difference was observed by increasing the AZO content while decreasing the graphite content, led to lower values of electrical conductivity, being around 0.7 times lower with increasing the AZO from 17 to 29%. This decrease was expected, since the graphite is a conductive filler added to improve the electrical conductivity of the samples, therefore, decreasing it, lower values are presented.

Furthermore, it is interesting to note that both samples processed by tape-casting showed very similar electrical conductivity values, despite having different

amounts of conductive fillers. The hypothesis is that this similarity could be explained mainly due to the difference in roughness of their surfaces, since the sample TC - 85% - Azo 17% has rougher surfaces than the TC - 70.8% - Azo 17%, as previously evidenced by Figure 18, which leads to greater difficulty in establishing contact points during measurement.

Meanwhile, as the 3D - 85% - Azo 17% present higher amount of conductive fillers than the 3D - 85% - Azo 29%, the one with the highest AZO content has lower electrical conductivity values, as expected.

Overall, according to the previous research [13], the carbon felt, a commonly used commercial electrode, has a value of 22 S/m, while the best value reached was 1.9 S/m in this work, showing a difference of 1 order of magnitude and that there are still improvements that should be made for better performance.

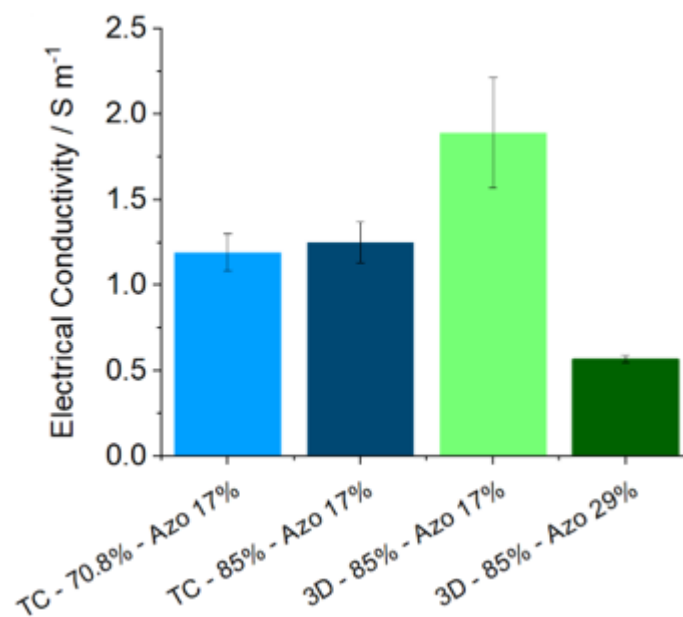


Figure 24: Electrical conductivity and its standard deviation from EIS. Source: Author.

Table 6: Electrical conductivity and its standard deviation from EIS. Source: Author.

Sample	σ (S/m)	SD
TC - 70.8% - Azo 17%	1.2	0.11
TC - 85% - Azo 17%	1.2	0.12
3D - 85% - Azo 17%	1.9	0.33
3D - 85% - Azo 29%	0.6	0.02

For the chemical stability analysis, all samples showed an insignificant/low dry weight variation. This corroborates to the fact that all organic molecules were eliminated during the pyrolysis above 600-800°C. Although a large quantity of carbon is expected due to the presence in graphite and carbon black on the composition, the dry weight of the samples did not vary it too much. The results are represented in Figure 25 and show that the sample remains stable over the time, only showing insignificant variations, probably during measurement on the scale. The chemical stability remains even after 21 days in simulated operating conditions for all samples.

The higher variation is about -3%, showed by the 3D - 85% - Azo 17% sample. This can be explained by the different geometry when compared to the others. While the other samples had rectangular and solid shape, it means, without infill, the 3D - 85% - Azo 17% sample had a lattice cuboid shape with infill, resulting in larger macroporosity due to the 3D structure and higher accessibility of the PBS solution, allowing for easier disintegration.

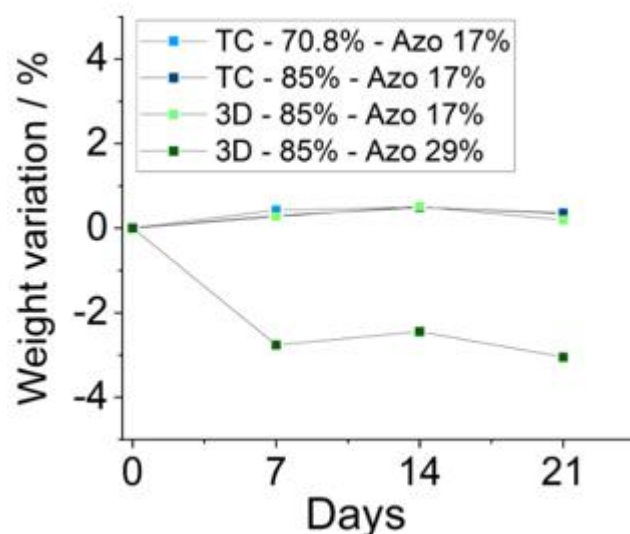


Figure 25: Chemical stability under PBS solution with pH 7 over 4 weeks. Source: Author.

6. CONCLUSION

The aim of the work was to develop 3D samples to later be used as an anode in MFC, which were made at first by adapting the composition previously used to tape cast [16], and then varying its geometry in lattice cuboids and cylindroids and the infill between rectilinear and honeycomb. In order to achieve satisfactory rheological properties for a 3D printability, four different solids loading from 70% to 85 wt.% were used. The composition with 85 wt.% showed a yield point of 1141.33 ± 32.33 Pa and maintained its structure stable when printing layer-by-layer during DIW. Nevertheless, the yield point showed an exponential increase with the increase of the solid loading, which should lead to unfeasible deposition pressure, higher than 300 Pa, if printing samples using solid loading above 85 wt.%.

Sequentially, the ink with 85 wt.% were 3D printed by using nozzle diameter size of 580 μm and speed of 10 mm/s, varying the applied pressure from 130 to 280 Pa, according to the time after cross-linking agent addition. This shows that although imidazole promotes good mechanical stability for the sample, processing the inks after long periods is not possible to the substantial increase of the degree of cross-linking. Nevertheless, the printing was successfully done using all geometries and different infills performed, but showed best results when rectilinear infill was used independently of the geometry, even though the 3D printed did not show strongly reliability on the resolution and accurateness to more complex infills, such as honeycomb.

To forecast a satisfactory bacteria adhesion and biofilm formation when applied as anodes in MFC, properties in terms of pore structure, such as pore size, open porosity and specific surface area were assessed. SEM images from the top surface, of the filaments did not show high volume of pores when increasing the AZO content from 17 to 23 and 29 wt.%. Although the mercury intrusion porosimetry showed an increase in open porosity of 5%, the pore surface did not open. Thus, to open the surface using the composition with solid loading of 85 wt.%, should be evaluate the use of other pore formation inducer agents, such as PMMA [77].

Nevertheless, the SEM images from the filaments and tape with 85 wt.% presented a roughness surface and no defects, as cracks. The 3D printed samples showed a perfect correspondence of the layer-by-layer deposition, indicating, in

qualitative terms, that the surface is promising to the biofilm formation and present a good mechanical stability.

Hg intrusion porosimetry indicated average pore window size mainly in macropores (>50 nm), influenced by the solid loading. The open porosity was influenced not only by the solid loading, but also by the higher amount of Azo for the 3D printed samples. The specific surface area increased more by changing the process from tape-casting to 3D printing – 3 times, than decreased by changing from 17 to 29 wt.% of AZO – 0.75 times. The value of 82,51 m²/g from the main sample, 3D - 85 wt.% - Azo17%, is high to materials pyrolyzed at 1000°C and more than 2 times higher when compared to TC - 70.8% - Azo 17%. These measurements were important to evaluate the good indicative for avoiding the pore clogging for having pores within filaments smaller than 100 µm and the proper bacterial colonization when using infill higher than 500 µm through the 3D structures. Therefore, samples that present higher average of pore window size within the filaments should be investigated.

Lastly, the functional properties gave a first idea of how the interaction between anode and bacteria will be, through the vapor adsorption analysis, showing a ratio water/n-heptane around 5, characteristic of a hydrophilic behavior. The chemical stability, using PBS solution at pH 7 to simulate the operational conditions, showed good performance with no loss of material, even after 4 weeks running. The EIS used to measure electrical conductivity, achieve the maximum at 1.89 S/m to the 3D - 85 wt.% - Azo17% sample, being 1.5 times higher than using tape-casting route and more than 3 times higher than using 29 wt.% of AZO. These results indicate that increasing the solid loading to 85 wt.%, maintaining the AZO content and using DIW as the process corresponds to the best performance.

Overall, the DIW processing proved to be better than tape-casting route. Although the open porosity increased by 5% when increasing the AZO content to 29 wt.%, the specific surface area and the electrical conductivity decreased by around 75% and 70% respectively, indicating that is better to maintain the same solid phase composition, but processing through 3D printing. Although the 3D sample has shown promise to the anode application, a final assessment can only be made once application tests have carried out in an MFC.

7. OUTLOOK

The following steps that can be done to experimentally assess whether the bacteria adhesion and biofilm formation will grow homogeneously distributed on the anode surface, analysis to immerse the sample into the simulated wastewater environment under controlled parameters would be indicated.

Furthermore, in order to potentialize the biofilm formation, a pore structure with higher volume of pores on the surface can be explored by replacing the AZO by other pore formation inducer, such as PMMA.

Lastly, the higher the electrical conductivity is the more efficient the anode will be, to this, 3D structures that promote the turbulent and laminar substrate flow should be designed, besides verify ink's compositions using more graphite content or even graphene to achieve better electrical properties and performance when applying to MFCs.

REFERENCES

- [1] Z. Caineng, Z. Qun, Z. Guosheng, X. Bo, Energy revolution: From a fossil energy era to a new energy era, *Natural Gas Industry B*, volume 3, 2016 1-11.
- [2] B.E. Logan, K. Rabaey, Conversion of Wastes into Bioelectricity and Chemicals by Using Microbial Electrochemical Technologies, *Science*, 337 (2012) 686.
- [3] V.B. Oliveira, M. Simoes, L.F. Melo, A.M.F.R. Pinto, Overview on the developments of microbial fuel cells, *Biochemical Engineering Journal*, 73 (2013) 53-64.
- [4] A. Janicek, Y. Fan, H. Liu, Design of microbial fuel cells for practical application: a review and analysis of scale-up studies, *Biofuels*, 5 (2014) 79-92.
- [5] A. Mehdinia, E. Ziaei, A. Jabbari, Multi-walled carbon nanotube/SnO₂ nanocomposite: a novel anode material for microbial fuel cells, *Electrochim Acta*, 130 (2014) 512-518.
- [6] C. Santoro, C. Arbizzani, B. Erable, I. Ieropoulos, Microbial fuel cells: From fundamentals to applications. A review, *J Power Sources*, 356 (2017) 225-244.
- [7] M.H. Zhou, M.L. Chi, J.M. Luo, H.H. He, T. Jin, An overview of electrode materials in microbial fuel cells, *J Power Sources*, 196 (2011) 4427-4435.
- [8] R. Thorne, H. Hu, K. Schneider, P. Bombelli, A. Fisher, L.M. Peter, A. Dent, P.J. Cameron, Porous ceramic anode materials for photo-microbial fuel cells, *Journal of Materials Chemistry*, 21 (2011) 18055-18060.
- [9] J. Winfield, I. Gajda, J. Greenman, I. Ieropoulos, A review into the use of ceramics in microbial fuel cells, *Bioresour Technol*, 215 (2016) 296-303
- [10] P. Moni, M. Wilhelm, K. Rezwan, The influence of carbon nanotubes and graphene oxide sheets on the morphology, porosity, surface characteristics and thermal and electrical properties of polysiloxane derived ceramics, *Rsc Adv*, 7 (2017) 37559-37567.
- [11] T. Prenzel, M. Wilhelm, K. Rezwan, Pyrolyzed polysiloxane membranes with tailorable hydrophobicity, porosity and high specific surface area, *Micropor Mesopor Mat*, 169 (2013) 160-167.
- [12] E. Ionescu, H.J. Kleebe, R. Riedel, Silicon-containing polymer-derived ceramic nanocomposites (PDC-NCs): preparative approaches and properties, *Chem Soc Rev*, 41 (2012) 5032-5052.

- [13] T. C. de Almeida e Silva, Polymer-derived SiOC Ceramics as New Electrode Materials for Microbial Fuel Cell Applications. 2019. Tese (Doctorate) – Materials science, University of Bremen, Bremen, 2019.
- [14] D. Schumacher, Porous Polymer-derived Ceramics by Solution-based Freeze Casting for Capillary Transport and Catalysis. 2020. Tese (Doctorate) – Materials Science, University of Bremen, Bremen, 2020.
- [15] J. C. Minardi, C. B. Demarchi, M. Mirdrikvand, M. N. Karim, W. Dreher, K. Rezwani, and M. Maas, 3D bioprinting of hydrogel/ceramic composites with hierarchical porosity, *Materials for life science*, 2022, 57:3662-3677.
- [16] P. H. da Rosa Braun, T. C. de Almeida e Silva, J. R. Quejigo, A. Kuchenbuch, K. Rezwani, F. Harnisch and M. Wilhelm, Impact of Surface Properties of Porous SiOC-Based Materials on the Performance of Geobacter Biofilm Anodes, *ChemElectroChem*, 2021, 8, 850-857
- [17] J. S. Reed, "Introduction to the Principles of Ceramic Processing". Wiley-Interscience, p. 1, 1988.
- [18] E. C. Subbarao, "Advanced Ceramics". *Transactions of the Indian Ceramic Society*, 46:3, p. 65-81, 1987.
- [19] K. Schelm, E. A. Morales, and M. Scheffler, "Mechanical and Surface-Chemical Properties of Polymer Derived Ceramic Replica Foams". *Materials*, vol. 12, no. 11. p. 1870, 2019.
- [20] M. Rahaman, "Ceramic Processing, Second Edition". CRC Press, p.15, 2017.
- [21] P. Colombo, G. Mera, R. Riedel, and G. D. Sorarù, "Polymer-derived ceramics: 40 years of research and innovation in advanced ceramics". *Journal of the American Ceramic Society*, vol. 93, p. 1805–1837, 2010.
- [22] P. Greil, "Polymer derived engineering ceramics". *Advanced engineering materials*, v. 2, n. 6, p. 339-348, 2000.
- [23] H. Rismani-Yazdi, S. M. Carver, A. D. Christy and O. H. Tuovinen, "Cathodic limitations in microbial fuel cells: An overview". *Power Sources*, n. 180, p. 683–694, 2008.

- [24] YAQOOB, A. A.; IBRAHIM, M. N. M.; GUERRERO-BARAJAS, C. Modern trend of anodes in microbial fuel cells (MFCs): An overview. *Environmental Technology & Innovation*, v. 23, p. 101579, ago. 2021.
- [25] SABA, B. et al. Sustainable power generation from bacterio-algal microbial fuel cells (MFCs): An overview. *Renewable and Sustainable Energy Reviews*, v. 73, p. 75–84, jun. 2017
- [26] KUMAR, R. et al. Exoelectrogens in microbial fuel cells toward bioelectricity generation: a review. *International Journal of Energy Research*, v. 39, n. 8, p. 1048–1067, 25 jun. 2015.
- [27] YAQOOB, A. A. et al. Outlook on the Role of Microbial Fuel Cells in Remediation of Environmental Pollutants with Electricity Generation. *Catalysts*, v. 10, n. 8, p. 819, 22 jul. 2020
- [28] Z.W. Du, H.R. Li and T.Y. Gu, “A state of the art review on microbial fuel cells: A promising technology for wastewater treatment and bioenergy”. *Biotechnol. Adv.* 25, p. 464–482, 2007.
- [29] FATEHBASHARZAD, P. et al. Microbial fuel cell applications for removal of petroleum hydrocarbon pollutants: A review. *Water Resources and Industry*, v. 28, p. 100178, dez. 2022
- [30] LJEŠEVIĆ, M. et al. Biodegradation of the aromatic fraction from petroleum diesel fuel by *Oerskovia* sp. followed by comprehensive GCxGC-TOF MS. *Journal of Hazardous Materials*, v. 363, p. 227–232, fev. 2019.
- [31] T. C. de Almeida e Silva, G. D. Bhowmick, M. M. Ghangrekar, M. Wilhelm, K. Rezwan, “SiOC-based polymer derived-ceramic porous anodes for microbial fuel cells”. *Biochemical Engineering Journal*, v. 148, p. 29-36, 2019.
- [32] LI, W.-W. et al. Recent advances in the separators for microbial fuel cells. *Bioresource Technology*, v. 102, n. 1, p. 244–252, jan. 2011).
- [33] C. T. Hyun, D. B. Ranjan, “A Mini-Review on Applications of 3D Printing for Microbial Electrochemical Technologies”. *Frontiers in Energy Research*, v. 9, 2021.

- [34] A. Zocca, P. Colombo, C. M. Gomes, and J. Günster, “Additive Manufacturing of Ceramics: Issues, Potentialities, and Opportunities”. *Journal of the American Ceramic Society*, vol. 98, no. 7. p. 1983–2001, 2015.
- [35] ISO/ASTM 52900:2015 – Additive manufacturing – General principles – Terminology. ASTM International.
- [36] JEFFERSON, J. M. E CHATTERJEE, DEBDUTTA. 2021. A review on polymeric materials in additive manufacturing. s.l. : *Materials Today Proceedings*, 2021. pp. 1349-1365. Vols. volume 46, part 2).
- [37] DAMINABO, S. C. et al. Fused deposition modeling-based additive manufacturing (3D printing): techniques for polymer material systems. *Materials Today Chemistry*, v. 16, p. 100248, jun. 2020)
- [38] FORSTER, A. M. *Materials Testing Standards for Additive Manufacturing of Polymer Materials: State of the Art and Standards Applicability*. Gaithersburg, MD: [s.n.]. Accessed on: <<https://nvlpubs.nist.gov/nistpubs/ir/2015/NIST.IR.8059.pdf>>.
- [39] LIGON, S. C. et al. Polymers for 3D Printing and Customized Additive Manufacturing. *Chemical Reviews*, v. 117, n. 15, p. 10212–10290, 9 ago. 2017.
- [40] LI, V. C.-F. et al. Cellulose nanocrystals support material for 3D printing complexly shaped structures via multi-materials-multi-methods printing. *Additive Manufacturing*, v. 28, p. 14–22, ago. 2019.
- [41] ALTIPARMAK, S. C. e XIAO, B. 2021. A market assessment of additive manufacturing potential for the aerospace industry. 2021: *Journal of Manufacturing Processes*, 2021. v. 68, p. 728–738.)
- [42] SCHLORDT, T. et al. Robocasting of alumina hollow filament lattice structures. *Journal of the European Ceramic Society*, v. 33, n. 15–16, p. 3243–3248, dez. 2013.
- [43] ZHOU, S. et al. Molecule editable 3D printed polymer-derived ceramics. *Coordination Chemistry Reviews*, v. 422, p. 213486, nov. 2020.
- [44] CUMPSTON, B. H. et al. Two-photon polymerization initiators for three-dimensional optical data storage and microfabrication. *Nature*, v. 398, n. 6722, p. 51–54, mar. 1999.

- [45] CHOUDHURY, D. et al. A 3D mammalian cell separator biochip. *Lab on a Chip*, v. 12, n. 5, p. 948, 2012.
- [46] ELSAYED, H. et al. Direct ink writing of silica-carbon-calcite composite scaffolds from a silicone resin and fillers. *Journal of the European Ceramic Society*, v. 38, n. 15, p. 5200–5207, dez. 2018.
- [47] TRAVITZKY, N. et al. Additive Manufacturing of Ceramic-Based Materials. *Advanced Engineering Materials*, v. 16, n. 6, p. 729–754, jun. 2014.
- [48] MEI, H. et al. 3D-printed oblique honeycomb Al₂O₃/SiC_w structure for electromagnetic wave absorption. *Chemical Engineering Journal*, v. 372, p. 940–945, set. 2019.
- [49] FRANCHIN, G. No Title. *American Ceramic Society Bulletin*, v. 96, n. 3, p. 15–23, 2017. ECKEL, Z. C. et al. Additive manufacturing of polymer-derived ceramics. *Science*, v. 351, n. 6268, p. 58–62, jan. 2016.
- [50] ECKEL, Z. C. et al. Additive manufacturing of polymer-derived ceramics. *Science*, v. 351, n. 6268, p. 58–62, jan. 2016.
- [51] TAO, X. et al. A facile method to prepare ZrC nanofibers by electrospinning and pyrolysis of polymeric precursors. *Ceramics International*, v. 43, n. 4, p. 3910–3914, mar. 2017.
- [52] TAO, X. et al. Fabrication of continuous ZrB₂ nanofibers derived from boron-containing polymeric precursors. *Journal of Alloys and Compounds*, v. 697, p. 318–325, mar. 2017.
- [53] FU, K. et al. Graphene Oxide-Based Electrode Inks for 3D-Printed Lithium-Ion Batteries. *Advanced Materials*, v. 28, n. 13, p. 2587–2594, abr. 2016.
- [54] CHEN, H. et al. 3D printing of SiC ceramic: Direct ink writing with a solution of preceramic polymers. *Journal of the European Ceramic Society*, v. 38, n. 16, p. 5294–5300, dez. 2018.
- [55] SHAHZAD, A.; LAZOGLU, I. Direct ink writing (DIW) of structural and functional ceramics: Recent achievements and future challenges. *Composites Part B: Engineering*, v. 225, p. 109249, nov. 2021.

- [56] GADDAM, A. et al. Robocasting and surface functionalization with highly bioactive glass of ZrO₂ scaffolds for load bearing applications. *Journal of the American Ceramic Society*, v. 105, n. 3, p. 1753–1764, 12 mar. 2022.
- [57] SMAY, J. E. et al. Directed Colloidal Assembly of 3D Periodic Structures. *Advanced Materials*, v. 14, n. 18, p. 1279–1283, 16 set. 2002.
- [58] HUR, H. et al. Material extrusion for ceramic additive manufacturing with polymer-free ceramic precursor binder. *Materials & Design*, v. 221, p. 110930, set. 2022.
- [59] PENG, E.; ZHANG, D.; DING, J. Ceramic Robocasting: Recent Achievements, Potential, and Future Developments. *Advanced Materials*, v. 30, n. 47, p. 1802404, nov. 2018.
- [60] CESARANO, J. A Review of Robocasting Technology. *MRS Proceedings*, v. 542, p. 133, 10 fev. 1998.
- [61] R. P. Chaudhary, C. Parameswaran, M. Idrees, A. S. Rasaki, C. Liu, Z. Chen, P. Colombo, “Additive manufacturing of polymer-derived ceramics: Materials, technologies, properties and potential applications”. *Progress in Materials Science*, v. 128, 2022.
- [62] HUANG, K. et al. 3D printing of polymer-derived SiOC with hierarchical and tunable porosity. *Additive Manufacturing*, v. 36, p. 101549, dez. 2020.
- [63] ROMÁN-MANSO, B. et al. Polymer-derived ceramic/graphene oxide architected composite with high electrical conductivity and enhanced thermal resistance. *Journal of the European Ceramic Society*, v. 38, n. 5, p. 2265–2271, maio 2018.
- [64] Feys, D.; Cepuritis, R.; Jacobsen, S.; Lesage, K.; Secrieru, E.; Yahia, A. Measuring Rheological Properties of Cement Pastes: Most Common Techniques, Procedures and Challenges. *RILEM Tech Lett* 2017, 2, 129-135.
- [65] S. K. Sharma, “Handbook of Materials Characterization || Scanning Electron Microscopy: Principle and Applications in Nanomaterials Characterization”. p. 113–145, 2018.
- [66] A. Abell, K. Willis and D. Lange, “Mercury intrusion porosimetry and image analysis of cement-based materials”. *Journal of colloid and interface science*, v. 211, n. 1, p. 39-44, 1999.

- [67] K.S.W. Sing, D.H. Everett, R.A.W. Haul, L. Moscou, R.A. Pierotti, J. Rouquérol, T. Siemienińska, Reporting Physisorption Data for Gas/Solid Systems With Special Reference to the Determination of Surface Area and Porosity.
- [68] J. Rouquerol, D. Avnir, C.W. Fairbridge, D.H. Everett, J.H. Haynes, N. Pernicone, J.D.F. Ramsay, K.S.W. Sing, K.K. Unger, Recommendations for the Characterization of Porous Solids, *Pure Appl Chem*, 66 (1994) 1739-1758.
- [69] S. Brunauer, P.H. Emmett, E. Teller, Adsorption of Gases in Multimolecular Layers, *J Am Chem Soc*, 60 (1938) 309-319.
- [70] BELSORP-mini, "Instruction manual". BEL Japan Inc. Ver.1.2.2, 12-18, 2009.
- [71] A.B.D. Cassie, S. Baxter, *Transactions of the Faraday Society* 40 (1944) 546-551.
- [72] T. Prenzel, T.L.M. Guedes, F. Schluter, M. Wilhelm, K. Rezwani, Tailoring surfaces of hybrid ceramics for gas adsorption - From alkanes to CO₂, *Sep Purif Technol*, 129 (2014) 80-89.
- [73] BARSOUKOV, E.; MACDONALD, J. R. *Impedance Spectroscopy: Theory, Experiment, and Applications*. [S.l.]: WILEY Interscience, 2005.
- [74] HE, Z.; MANSFELD, F. Exploring the use of electrochemical impedance spectroscopy (EIS) in microbial fuel cell studies, Los Angeles, v. 2, 2009. p. 215-219.
- [75] OPARAODU, K. O.; OKPOKWASILI, G. C. Comparison of Percentage Weight Loss and Corrosion Rate Trends in Different Metal Coupons from two Soil Environments, Nigeria, v. 2, n. 5, 2014. p. 243-249.
- [76] XIAO-GANG, L. et al. Characteristics of graphite felt electrode electrochemically oxidized vanadium redox battery application, China, v. 17, 2007. P. 195-199.
- [77] A. B. Haugen, J. Gurauskis, A. Kaiser, M. Sogaard, Graphite and PMMA as pore formers for thermoplastic extrusion of porous 3Y-TZP oxygen transport membrane supports, *Journal of the European Ceramic Society*, volume 37, 2017. 1039-1047.

APENNDIX A – History of The Institute


Founded in 1994 as an endowment chair, the “Ceramics” chair was headed by Prof. Grathwohl till 2009 before retirement. Hereafter, in October 2009, this chair was merged together with the “Bioceramics” group which was a Junior professorship position held by Prof. Rezwan since 2006. After the successful merging of both chairs, the new chair is now called “Advanced Ceramics” with Prof. Rezwan being in charge.

We investigate, develop and engineer advanced ceramic materials for applications in the areas of biomaterials engineering, environmental engineering, energy harvesting devices and aerospace. Advanced ceramic materials feature a variety of superior properties such as hardness, wear-, corrosion- and high temperature resistance. Our group's current research interests focus on:

- Novel Processing Routes for Biofunctional Ceramics
- Precursor derived Ceramics and Ceramers
- Functionalization and Assembly of Ceramic Nanoparticles
- Advanced Ceramic Composites

Available at: <https://www.ceramics.uni-bremen.de/> (accessed on 19/09/2022)

APENNDIX B – Timetable Schedule

	Timetable Schedule (04/01/2022 a 09/30/2022)																							
	Bruno Toselli																							
Month	April				May				June				July				August				September			
Week	1	2	3	4	1	2	3	4	1	2	3	4	1	2	3	4	1	2	3	4	1	2	3	4
Background literature	X	X	X	X	X	X	X	X	X	X	X	X	X	X	X	X	X	X	X	X	X	X	X	X
Sample preparation	X	X	X	X	X	X	X		X	X	X			X	X	X	X	X	X				X	
Syringe test	X	X					X		X															
Freeze drying		X		X		X	X		X															
3D printing		X		X		X	X		X	X	X			X	X	X	X	X	X				X	
Tape-casting																		X	X			X		
Rheology analysis					X	X	X		X	X						X	X		X					
Pyrolysis		X		X		X	X		X	X							X		X					X
Hg intrusion								X			X												X	X
SEM analysis								X		X	X									X				X
BET analysis									X	X						X	X	X				X	X	
Vapor adsorption																	X	X		X	X			
EIS																	X	X		X	X	X	X	X
Chemical stability																		x	X	X	X	X	X	X
Report				X				X		X	X	X				X				X			X	X